Available online at www.sciencedirect.com

ScienceDirect

Geochimica et Cosmochimica Acta 302 (2021) 18–45

Geochimica et Cosmochimica Acta

www.elsevier.com/locate/gca

Iron, magnesium, and titanium isotopic fractionations between garnet, ilmenite, fayalite, biotite, and tourmaline: Results from NRIXS, *ab initio*, and study of mineral separates from the Moosilauke metapelite

Nicole X. Nie [a,b,c,*], Nicolas Dauphas [a,b], Esen E. Alp [d], Hao Zeng [a,b], Corliss K. Sio [e], Justin Y. Hu [a,b], Xi Chen [a,b], Sarah M. Aarons [a,b,f], Zhe Zhang [a,b], Heng-Ci Tian [g,h], Da Wang [c], Kelsey B. Prissel [c,i], Jennika Greer [b,j], Wenli Bi [d], Michael Y. Hu [d], Jiyong Zhao [d], Anat Shahar [c], Mathieu Roskosz [k], Fang-Zhen Teng [h], Michael J. Krawczynski [i], Philipp R. Heck [b,j], Frank S. Spear [l]

[a] *Origins Laboratory, Department of the Geophysical Sciences and Enrico Fermi Institute, The University of Chicago, Chicago, IL 60637, United States*

[b] *Chicago Center for Cosmochemistry, The University of Chicago, Chicago, IL 60637, United States*

[c] *Earth and Planets Laboratory, Carnegie Institution for Science, Washington, DC 20015, United States*

[d] *Advanced Photon Source, Argonne National Laboratory, 9700 South Cass Avenue, Argonne, IL 60439, United States*

[e] *Lawrence Livermore National Laboratory, 7000 East Ave L-231, Livermore, CA 94550, United States*

[f] *Scripps Institution of Oceanography, UC San Diego, La Jolla, CA 92093-0220, United States*

[g] *Key Laboratory of Earth and Planetary Physics, Institute of Geology and Geophysics, Chinese Academy of Sciences, Beijing 100029, China*

[h] *Isotope Laboratory, Department of Earth and Space Sciences, University of Washington, Seattle, WA 98195, United States*

[i] *McDonnell Center for the Space Sciences and Department of Earth and Planetary Sciences, Washington University in St. Louis, 1 Brookings Drive, St. Louis, MO 63123, United States*

[j] *Robert A. Pritzker Center for Meteoritics and Polar Studies, The Field Museum of Natural History, Chicago, IL 60605, United States*

[k] *IMPMC, CNRS, UMR 7590, Sorbonne Universités, Université Pierre et Marie Curie, Muséum National d'Histoire Naturelle, CP 52, 57 rue Cuvier, Paris F-75231, France*

[l] *Department of Earth and Environmental Sciences, Rensselaer Polytechnic Institute, 110 8th Street, Troy, NY 12180, United States*

Received 12 August 2020; accepted in revised form 11 March 2021; available online 23 March 2021

Abstract

Interpreting isotopic signatures documented in natural rocks requires knowledge of equilibrium isotopic fractionation factors. Here, we determine equilibrium Fe isotope fractionation factors between several common rock-forming minerals using a comparative approach involving three independent methods: (*i*) isotopic analyses of natural minerals from a metapelite from Mt. Moosilauke, New Hampshire, for which equilibration temperature and pressure are well constrained to be near the aluminosilicate triple point ($T \simeq 500$ °C, $P \simeq 4$ kbar), (*ii*) Nuclear Resonant Inelastic X-ray Scattering (NRIXS) measurements of Fe force constants of minerals, and (*iii*) Density Functional Theory (DFT) *ab initio* calculations of Fe force constants of minerals.

The minerals studied for Fe isotopes include, in increasing order of their β-factors: garnet < ilmenite ≈ fayalite < biotite < tourmaline < muscovite ≈ plagioclase. Some of this ordering is affected by the presence of Fe^{3+} in the minerals, which

* Corresponding author.
E-mail address: nnie@carnegiescience.edu (N.X. Nie).

https://doi.org/10.1016/j.gca.2021.03.014

tends to form stiffer bonds and be associated with heavy Fe isotope enrichments relative to Fe^{2+}. We are, however, able to assess the magnitude of the effect of the ratio $Fe^{3+}/\Sigma Fe$ on equilibrium fractionation factors, notably on the ilmenite-hematite solid solution. Equilibrium Fe isotopic fractionation factors between garnet, ilmenite, biotite, tourmaline and fayalite are determined. We also report Mg and Ti isotopic compositions of selected Moosilauke minerals that allow us to better constrain the equilibrium fractionation factors for garnet-biotite-tourmaline (Mg isotopes) and biotite-ilmenite (Ti isotopes).

We show how the newly determined equilibrium fractionation factors can be used to address diverse problems in Earth and planetary sciences, notably (*i*) Fe and Mg isotopic fractionation during anatexis, (*ii*) Fe isotopic fractionation in lunar ilmenite, and (*iii*) Ti isotopic fractionation during fluvial transport of minerals.

Keywords: Iron isotopes; Mg isotopes; Ti isotopes; Moosilauke Metapelite; NRIXS; *Ab initio* calculations

1. INTRODUCTION

Recent years have seen rapid growth in the applications of non-traditional stable isotopes to diverse topics ranging from cosmochemistry to medicine (Teng et al., 2017 and references therein). The iron isotope system has been extensively studied due to the ubiquity of Fe in most rocks and its variable oxidation states. It has been used to trace processes covering both high-temperature (*e.g.*, early solar system formation, planetary accretion, magmatic differentiation, and core formation) and low-temperature processes (*e.g.*, iron absorption in humans, surface weathering, iron cycling in the oceans and sediments) (Dauphas et al., 2017 and references therein). To interpret iron isotopic variations in nature, it is crucial to know how Fe isotopes are fractionated between coexisting phases at equilibrium. In some systems, these equilibrium isotopic fractionation factors are poorly constrained, or published results are inconsistent, which leads to ambiguities in interpretations.

Four independent methods can be used to determine equilibrium Fe isotope fractionation factors (Dauphas et al., 2017; Shahar et al., 2017): (*i*) One can measure natural co-existing minerals (*e.g.*, Beard and Johnson, 2004; Huang et al., 2011; Wu et al., 2017; Ye et al., 2020) but it can be difficult to assess whether the minerals are in isotopic equilibrium, and even if they are, the equilibration temperature can be difficult to assess. Sample selection is thus critical. (*ii*) One can measure the isotopic compositions of the products of laboratory experiments where the coexisting phases have achieved equilibrium or any departure thereof can be corrected for (*e.g.*, Skulan et al., 2002; Welch et al., 2003; Shahar et al., 2008, 2015; Beard et al., 2010; Elardo and Shahar, 2017; Sossi and O'Neill, 2017; Prissel et al., 2018). Equilibration between minerals has to be evaluated carefully because kinetic effects can cause large isotopic fractionation and therefore mask equilibrium fractionation. (*iii*) One can use the synchrotron radiation spectroscopic technique of nuclear resonant inelastic X-ray scattering (NRIXS) to derive mean kinetic energy or mean force constant of Fe in minerals, from which fractionation factors between minerals can be calculated (*e.g.*, Polyakov et al., 2007; Dauphas et al., 2012, 2018; Blanchard et al., 2015; Roskosz et al., 2015). This technique can only be applied to Mössbauer isotopes such as ^{57}Fe, so not all elements can be measured using this method. The technique is relatively new, but it has been applied to isotopic fractionations of Fe and Sn (*e.g.*, Dauphas et al., 2012; Blanchard et al., 2015; Roskosz et al., 2015, 2020, Shahar et al., 2016) and can also be applied to others such as Kr, Eu, and Dy (Dauphas et al., 2018). (*iv*) One can perform *ab initio* calculations using density-functional theory (DFT), from which vibrational frequencies can be obtained to calculate isotope fractionation factors (*e.g.*, Schauble, 2004; Hill and Schauble, 2008; Ottonello and Zuccolini, 2009; Rustad and Dixon, 2009; Fujii et al., 2014; Blanchard et al., 2017).

All the approaches highlighted above have strengths and weaknesses. We have therefore performed a comprehensive study to evaluate the degree of consistency between these different methods and their ability to correctly predict isotope fractionation factors. In the present work, we have studied equilibrium isotope fractionation factors (mainly Fe, as well as Mg and Ti for selected phases) between several rock-forming minerals using three independent methods. The goals of this study are to (*i*) more precisely constrain equilibrium fractionation factors and (*ii*) test the consistency between various approaches. We first measured the Fe isotopic compositions of minerals from a pelitic schist from Mt. Moosilauke, New Hampshire, for which the temperature and pressure conditions are very well constrained to be very near the aluminosilicate (Al_2SiO_5) triple point ($T \simeq 500$ °C, $P \simeq 4$ kbar; Hodges and Spear, 1982). This rock was used to calibrate many geothermobarometers based on mineral paragenesis and element distribution between coexisting minerals. It is thus particularly well suited for calibrating equilibrium isotopic fractionation factors. We have also performed NRIXS measurements to determine the Fe force constants of these minerals and the equilibrium isotopic fractionation factors between them. Finally, we performed *ab initio* calculations using a DFT approach to calculate Fe force constants and isotopic fractionation factors. The results from the three methods are compared with each other to test their consistency and to ensure that the equilibrium fractionation factors thus derived are reliable.

In this work we study several minerals, including garnet, ilmenite, biotite, tourmaline, muscovite, plagioclase, quartz (these minerals are present in the pelitic schist from Moosilauke) and olivine (olivine is not present in the schist but NRIXS and *ab initio* calculations were performed on it for comparison purposes). Applications of these equilibrium fractionation factors to metamorphic and igneous petrology are discussed.

2. SAMPLES AND METHODS

2.1. Natural minerals from Mt. Moosilauke

Measuring naturally co-existing minerals provides a relatively straightforward way of constraining equilibrium isotope fractionation factors. Sample selection is however critical, because not all co-existing minerals are in isotopic equilibrium in metamorphic and igneous rocks, and the magnitude of equilibrium isotopic fractionation factors between two phases decreases with increasing equilibration temperature ($\Delta_{A\text{-}B} \propto 1/T^2$; pressure has negligible effect compared to temperature, at least in conditions relevant to crustal processes; Bigeleisen and Mayer, 1947). Therefore, knowing precisely the equilibration temperatures of phases is important to make meaningful use of isotopic differences measured between minerals.

In this work, we address the two difficulties by studying a carefully selected pelitic schist sample (R71-90) from Mt. Moosilauke, New Hampshire (Hodges and Spear, 1982). All chemical and mineralogical evidence points to a mineral paragenesis that is in chemical equilibrium, including lack of zoning (Hodges and Spear, 1982). This bodes well for isotopic fractionations of the minerals recording equilibrium conditions. Another virtue of studying Moosilauke minerals is that the metamorphic temperature and pressure for chemical equilibration are well constrained. The coexistence of aluminosilicate minerals (andalusite, kyanite, and sillimanite) in the vicinity constrains the equilibrium temperature and pressure to be very near the aluminosilicate triple point (Fig. 1; Rumble, 1973; Hodges and Spear, 1982). Hodges and Spear (1982) were thus able to use the minerals to calibrate a variety of geothermometers and geobarometers. To our knowledge, this is the first study using Moosilauke samples for calibrating equilibrium isotopic fractionation factors. The pelitic schist sample R71-90 in this work is from the same outcrop as the sample R71-90A studied in Hodges and Spear (1982); the one that is closest to the aluminosilicate triple point. Hodges and Spear (1982) and previous work (Holdaway, 1971) considered P-T conditions of 500 °C and 4 kbar at the triple point. Later work reevaluated the P-T condition of the triple point to be at ~550 °C and 4.5 kbar (Pattison, 1992). This temperature and pressure difference will not affect much our estimated isotope fractionation factors. In this work we adopt 500 °C as the equilibration temperature to calculate isotope fractionation factors between minerals (Section 4). Quartz, biotite and muscovite are the major minerals in schist R71-90, plagioclase, ilmenite and garnet are abundant but in lesser amounts. Tourmaline was also observed but in low abundance.

A small, fresh chip of R71-90 obtained by crushing a larger piece of the rock was ground gently in a pre-cleaned agate mortar, then sieved using several mesh sizes to obtain a fraction containing mostly single minerals (~tens to hundreds of micron). Before handpicking minerals, phyllosilicates (biotite and muscovite) were mechanically separated from other more round-shaped minerals (mainly quartz, plagioclase and garnet). Specifically, the two types of minerals can be separated by tilting and tapping paper on which the mineral mixture is deposited. Round grain minerals roll off the paper while phyllosilicates stick to the paper. This step produced a clean phyllosilicate separate, facilitating further mineral separation under a microscope.

Seven minerals were separated manually under an optical microscope, including garnet, ilmenite, biotite, muscovite, plagioclase, tourmaline and quartz (Fig. 1). A small fraction of the picked minerals was mounted in epoxy, checked under a scanning electron microscope (SEM) and characterized with energy dispersive x-ray spectroscopy (EDS). A fraction of the picked minerals with the highest purity was selected for Fe, Mg and Ti isotope

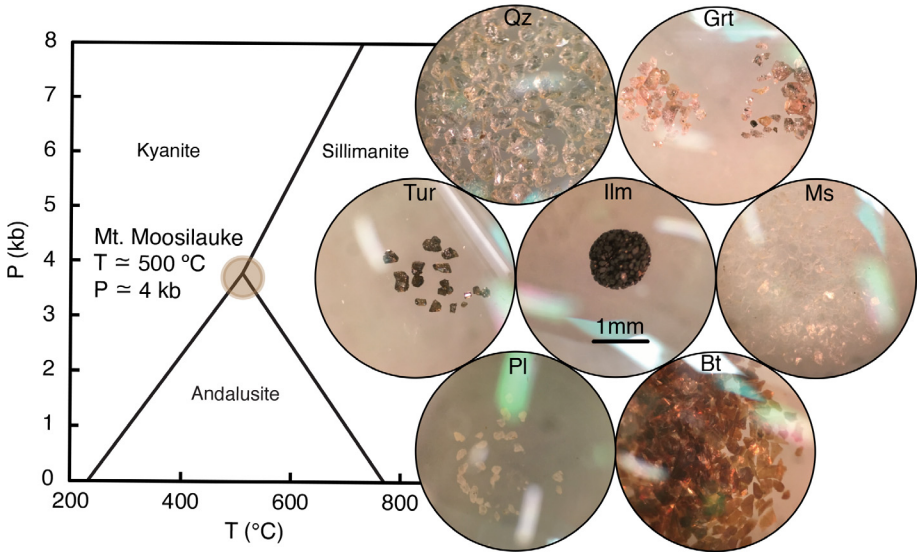

Fig. 1. Minerals separated from pelitic schist R71-90. The minerals underwent chemical equilibrium at P-T condition very near the aluminosilicate triple point (T ≃ 500 °C, P ≃ 4 kbar). Qz: quartz; Grt: garnet; Tur: tourmaline; Ilm: ilmenite; Ms: muscovite; Pl: plagioclase; Bt: biotite.

measurements (Tables 1 and 2; Figs. 2 and 3). Quartz was present as colorless and yellowish grains, and both were picked separately and measured for their Fe isotopes, but the Fe amount in quartz is extremely low and the measured Fe isotopic composition is surely affected by other Fe-bearing minerals present as inclusions or adhering to the surface of the quartz grains. We report the quartz data for the sake of completeness but make no use of them. The entire mineral separation procedure was performed on a second fresh chip from the same rock to check the reproducibility of Fe isotope measurements, and the results on mineral separates 1 and 2 are reported in Table 1.

For isotopic analysis, about 1 mg of each mineral was dissolved using mixtures of HF-HNO_3-$HClO_4$ following a protocol described previously (Dauphas et al., 2004, 2009; Dauphas and Rouxel, 2006). Digestion residues and minerals that are not easily digested (*e.g.*, ilmenite) were transferred to Parr bombs for digestion with a concentrated HF/HNO_3 (28 M and 15 M respectively mixed in a 2:1 proportion) mixture heated at 170 °C in an oven for 3 days. For each mineral solution, half was used for Fe isotopic analysis and half was used for Mg isotopic analysis.

The method for Fe chemical separation and isotopic analysis is the one routinely used in the Origins Lab at the University of Chicago (Dauphas et al., 2004, 2009; Dauphas and Rouxel, 2006). Iron is separated from matrix elements by passing samples in 6 N HCl through AG1-X8 (200–400 mesh) resin. Matrix elements and Fe are eluted with 6 N HCl and 0.4 N HCl respectively. The procedure was performed twice. The purified Fe was evaporated to dryness and taken up in 2% HNO_3 (~0.3 M) for Fe isotopic analysis. Iron isotopic analyses were carried out on a Thermo Scientific Neptune MC-ICPMS upgraded to Neptune Plus specifications in the Origins Lab at the University of Chicago. A quartz SSI cyclonic/Scott dual spray chamber was used as the sample introduction system, and standard-sample bracketing was used to correct for instrumental fractionation. All Fe isotope data were bracketed and expressed relative to IRMM-524, whose isotopic composition is identical to IRMM-014 (Craddock and Dauphas, 2010).

Magnesium separation and isotopic analysis were carried out at the Isotope Laboratory of the University of Washington. Magnesium was separated using AG50W-X8 cation exchange resin in 1 M HNO_3 and the elution procedure was repeated for another time. Magnesium isotopic composition was measured using a Nu Plasma MC-ICPMS at the University of Washington in low resolution mode and is reported relative to reference standard DSM-3. Detailed procedures have been reported previously (Teng and Yang, 2014; Teng et al., 2015).

Ilmenite, biotite, and the bulk rock were measured for their Ti isotopic compositions, which are reported in Table 2. Sample digestion, Ti separation, and Ti isotopic analysis followed the method described in Greber et al. (2017a), which is slightly modified from an earlier procedure (Zhang et al., 2011; Millet and Dauphas, 2014). Alkali flux fusion with lithium metaborate was used for complete dissolution of the samples based on a procedure outlined in Pourmand et al. (2012) and modified for Ti (Greber et al., 2017a). Sample solutions were spiked with an ideal proportion of ^{47}Ti-^{49}Ti double spike as described in Millet and Dauphas (2014) before Ti purification. The chemical procedure for Ti purification was outlined in Zhang et al. (2011). Briefly, Ti was separated from the matrix through a two-step ion-exchange chromatography. The first step used a 2 mL TODGA column to separate Ti from matrix elements, and in a second stage Ti was purified with 0.8 mL of AG1-X8 resin. Titanium isotopic compositions were analyzed using the Origins Lab MC-ICPMS at the University of Chicago, using an Aridus sample introduction system together with X skimmer and Jet sampler cones, in medium resolution mode on peak shoulders to avoid potential molecular interferences. Titanium isotopic compositions were measured relative to a reference standard named Origins Laboratory Ti standard (OL-Ti), whose composition is close to the bulk silicate Earth and chondrites (Millet et al., 2016; Greber et al., 2017a). The Fe, Mg and Ti isotopic data in this study are reported using the conventional δ-notation as follows (Tables 1 and 2; Figs. 2 and 3),

$$\delta^{56}\mathrm{Fe}(‰) = 1000\left[\left(\frac{^{56}\mathrm{Fe}}{^{54}\mathrm{Fe}}\right)_{\mathrm{sample}} / \left(\frac{^{56}\mathrm{Fe}}{^{54}\mathrm{Fe}}\right)_{\mathrm{IRMM-014}} - 1\right], \quad (1)$$

$$\delta^{26}\mathrm{Mg}(‰) = 1000\left[\left(\frac{^{26}\mathrm{Mg}}{^{24}\mathrm{Mg}}\right)_{\mathrm{sample}} / \left(\frac{^{26}\mathrm{Mg}}{^{24}\mathrm{Mg}}\right)_{\mathrm{DSM-3}} - 1\right], \quad (2)$$

$$\delta^{49}\mathrm{Ti}(‰) = 1000\left[\left(\frac{^{49}\mathrm{Ti}}{^{47}\mathrm{Ti}}\right)_{\mathrm{sample}} / \left(\frac{^{49}\mathrm{Ti}}{^{47}\mathrm{Ti}}\right)_{\mathrm{OL-Ti}} - 1\right]. \quad (3)$$

2.2. NRIXS measurements of the Fe reduced partition function ratios (β-factors) of minerals

Natural minerals were measured for their iron phonon density of states using NRIXS. The minerals are Fe-rich endmember minerals of the ones encountered in Moosilauke, for maximizing the ^{57}Fe abundance as the NRIXS technique can only probe ^{57}Fe (the Mössbauer isotope of Fe), which has a natural abundance of only 2.119 %. NRIXS uses the nuclear transition of Mössbauer isotopes to probe the vibration modes of chemical bonds in solids, from which phonon density of states (PDOS), reduced partition function ratios (1000 lnβ) and mean force constants ($\langle F \rangle$) can be derived (Seto et al., 1995; Sturhahn et al., 1995; Chumakov and Sturhahn, 1999; Alp et al., 2003; Sturhahn and Jackson, 2007; Dauphas et al., 2018). Equilibrium isotope fractionations between minerals can be calculated using the PDOS through the kinetic energy (Polyakov et al., 2005) or a moment expansion of NRIXS spectrum (phonon excitation probability density function), whose first term is related to the mean force constant of the Fe bonds (Dauphas et al., 2012, 2018).

Five natural minerals of high purity and homogeneity were chosen for NRIXS measurements (Table 3), including **almandine** (Fe-rich endmember of garnet) from Garnet Hill

Table 1
Fe isotopic compositions of Moosilauke mineral separates (relative to IRMM-014).

	Mineral separates 1				Mineral separates 2				Weighted average of two separates				Mineral–garnet fractionation (500 °C)			
	δ^{56}Fe	95% c.i.	δ^{57}Fe	95% c.i.	δ^{56}Fe	95% c.i.	δ^{57}Fe	95% c.i.	δ^{56}Fe	95% c.i.	δ^{57}Fe	95% c.i.	Δ^{56}Fe	95% c.i.	Δ^{57}Fe	95% c.i.
Garnet	−0.223	0.035	−0.322	0.066	−0.211	0.025	−0.305	0.038	−0.215	0.020	−0.309	0.033	0	0	0	0
Ilmenite	−0.169	0.035	−0.260	0.066	−0.174	0.022	−0.251	0.032	−0.172	0.019	−0.253	0.028	0.042	0.028	0.056	0.044
Biotite	0.092	0.035	0.146	0.066	0.099	0.025	0.147	0.038	0.097	0.020	0.147	0.033	0.311	0.029	0.456	0.047
Tourmaline	0.189	0.040	0.249	0.080	0.204	0.026	0.316	0.047	0.200	0.022	0.299	0.040	0.414	0.030	0.608	0.052
Muscovite	0.297	0.042	0.437	0.083	0.362	0.026	0.507	0.055	0.344	0.022	0.486	0.046	0.559	0.030	0.795	0.057
Plagioclase	0.351	0.070	0.417	0.095	0.206	0.070	0.232	0.085	0.278	0.049	0.314	0.063	0.493	0.053	0.623	0.071
Quartz (colorless)	0.403	0.040	0.521	0.106	n.d.	n.d.	n.d.	n.d.								
Quartz (yellow)	0.267	0.037	0.334	0.070	n.d.	n.d.	n.d.	n.d.								
Bulk					0.102	0.020	0.138	0.029	0.102	0.020	0.138	0.029	0.317	0.028	0.447	0.044

n.d. not determined.

Ely Nevada, **ilmenite (NMNH96189**; ilmenite microbeam standard), **annite (M9297**; Fe-rich endmember of mica) originally from Rockfort, Massachusetts USA (provided by the Field Museum, Chicago), **schorl** (Fe-rich endmember of tourmaline) from Karibib District, Erongo Region, Namibia, and **fayalite (M7652**; Fe-endmember of olivine from Rockfort, Massachusetts USA; provided by the Field Museum). Fayalite is not present in Moosilauke but was measured as we had previously studied a synthetic ^{57}Fe-doped forsterite (Dauphas et al., 2014) and wanted to assess the quality of PDOS measurements of undoped natural minerals.

Each mineral was ground to a fine powder using a cleaned agate mortar to minimize the effect of crystal orientation. The sample powder was then loaded into a 2 mm diameter Kapton capillary for NRIXS measurements. The measurements were performed at sector 3ID of the Advanced Photon Source (APS) at the Argonne National Laboratory. All measurements were at room pressure and temperature. X-rays with energy around 14.4125 keV (the nominal nuclear resonance energy of ^{57}Fe) were used to excite ^{57}Fe into a nuclear excited state. By applying appropriate time discrimination, only the scattered X-rays produced in the de-excitation of ^{57}Fe were measured using Avalanche Photodiodes. Details on the theory and method of Fe NRIXS measurement have been explained in previous work (Seto et al., 1995; Sturhahn et al., 1995; Chumakov and Sturhahn, 1999; Sturhahn and Jackson, 2007; Dauphas et al., 2012, 2018). By varying the energy of the incident X-rays around the nominal resonance energy and measuring the flux on resonantly scattered X-rays, one measures the phonon excitation probability density function $S(E)$, which through further data reduction and Log-Fourier transform yields the iron PDOS $g(E)$ (Sturhahn et al., 1995; Chumakov and Sturhahn, 1999; Dauphas et al., 2012). The reason why a nuclear transition can be used to probe lattice vibrations is that excitation of ^{57}Fe can happen outside of the nominal resonance energy of this nuclide when the lattice either absorbs or provides energy in the form of phonon creation or annihilation, allowing the excitation to occur even when the energy is either higher or lower than the resonance energy. The energy resolution of the incident X-ray beam (full width at half maximum) was ~1 meV. The beam was focused horizontally to a size of 25 μm while unfocused vertically in a size of 0.4 mm. The scans spanning typical energy ranges of −120 to +160 meV were acquired by varying the energy of the incident beam in increments of 0.25 meV. Data acquisition at each energy step lasted for 3 s, and several complete scans were processed for each sample, resulting in a total acquisition time at each energy of 90 s for a total duration of ~28 hr for each sample. The motivation for the broad energy scans is to monitor the counts in the energy tails of the spectrum that are used for background correction (Dauphas et al., 2018). Data reduction and calculation of the PDOS and all the quantities that can be derived from both $S(E)$ and $g(E)$ were performed using the SciPhon software (Dauphas et al., 2018). We can in particular calculate reduced partition function ratio as a polynomial expansion of the inverse of the square of the temperature

Table 2
Mg and Ti isotopic compositions of Moosilauke minerals (500 °C).

	Mg isotopes (relative to DSM-3)				Ti isotopes (relative to OL-Ti)	
	$\delta^{26/24}$Mg	2SD	$\delta^{25/24}$Mg	2SD	$\delta^{49/47}$Ti	95% c.i.
Garnet	−1.541	0.067	−0.801	0.060	n.d.	n.d.
Ilmenite	n.d.	n.d.	n.d.	n.d.	0.054	0.012
Biotite	−0.146	0.045	−0.066	0.045	0.431	0.013
Tourmaline	0.259	0.045	0.116	0.045	n.d.	n.d.
Bulk	−0.130	0.044	−0.037	0.041	0.231	0.016

n.d. not determined.

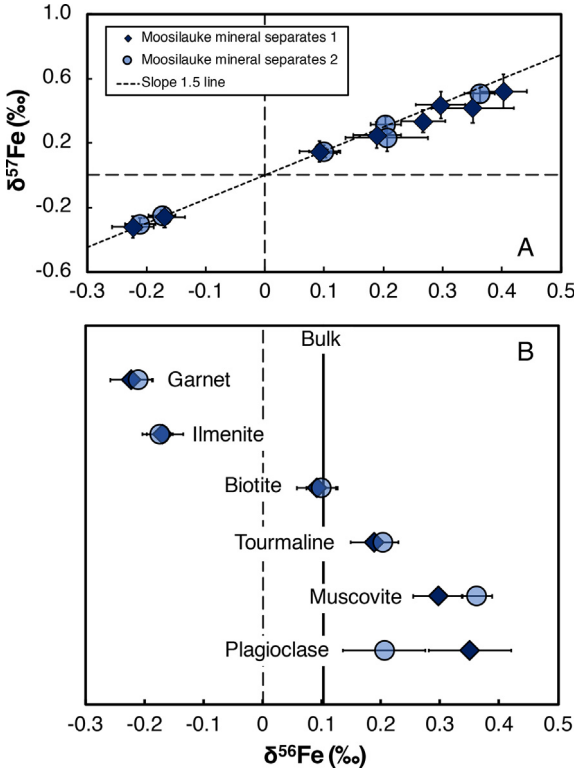

Fig. 2. Iron isotopic compositions of minerals picked from pelitic schist R71-90 from Mt. Moosilauke, New Hampshire. Two groups of minerals (mineral separates 1 and 2; Table 1) were separated from two rock chips of the same rock using the same method. (A) Iron isotopic compositions shown as a three-isotope plot. All data points following the slope 1.5 line (mass-dependent isotope fractionation line) indicates that the Fe isotope measurements did not suffer from isobaric interferences even for the most Fe-depleted samples (*i.e.*, muscovite and plagioclase). (B) δ^{56}Fe values of the two groups of separated minerals. The two datasets (light and dark blue symbols) show consistent Fe isotopic compositions except for plagioclase, which is attributed to the fact that plagioclase contains extremely small amount of Fe and its Fe isotopic composition can be easily affected by the presence of impurities.

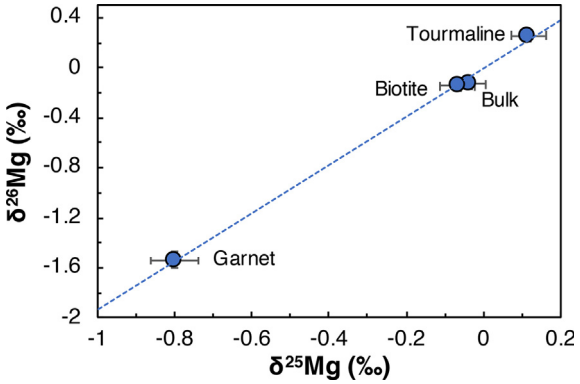

Fig. 3. Magnesium isotopic compositions of minerals picked from the pelitic schist R71-90 from Mt. Moosilauke, New Hampshire (Table 2).

(T is in K) with the coefficients in the expansion given by the moments of $g(E)$ or $S(E)$ (Dauphas et al., 2012; Hu et al., 2013),

$$1000\ln\beta\left({}^{56}\mathrm{Fe}/{}^{54}\mathrm{Fe}\right) \simeq \frac{A_1}{T^2}+\frac{A_2}{T^4}+\frac{A_3}{T^6} \quad (4)$$

At high temperature, this equation can well be approximated using the force constant as,

$$1000\ln\beta\left({}^{56}\mathrm{Fe}/{}^{54}\mathrm{Fe}\right) \simeq B_1\frac{\langle F\rangle}{T^2}-B_2\frac{\langle F\rangle^2}{T^4} \quad (5)$$

with $\langle F\rangle$ the mean force constant of the iron bonds (in N/m), $B_1 = 2904$ and B_2 is a constant depending on the shape of the PDOS (Blanchard et al., 2015). For iron in most minerals, $B_2 \simeq 52000$ (Dauphas et al., 2018). The virture of using Eq. (5) is that B_2, although slightly different for different minerals, does not change much (as shown in Table 3), allowing one to estimate β-factors when only force constant is known (Dauphas et al., 2017). The values of A_1, A_2, A_3, B_1, B_2 and $\langle F\rangle$ are compiled in Table 3. The other quantities that can be derived from $g(E)$ and $S(E)$ are also provided in the table. At temperatures above ~400 °C, β-factors can be well appoximated by the first terms in Eqs. 4 or 5. For lower temperatures, reduced partition function ratios can be calculated using Eq. (4) and the coefficients A_1, A_2, A_3 provided in Table 3. At a given temperature, the equilibrium Fe isotope fractionation factor between two phases is expressed as the difference between their reduced partition function ratios through,

$$\Delta_{A-B} = \delta_A - \delta_B = 1000ln\beta_A - 1000ln\beta_B \quad (6)$$

2.3. *Ab initio* calculations

The reduced partition function ratios of almandine, ilmenite, annite, schorl and fayalite were calculated using

Table 3
Mineral properties derived from NRIXS measurements.

	Almandine (Garnet Hill, Ely, Nevada)	Ilmenite (NMNH96189)	Annite (M9297, Rockfort, Massachusetts)	Schorl (Erongo Region, Namibia)	Fayalite (M7652, Rockport, Massachusetts)
Parameters from *S*					
Temperature from detailed balance (K)	273	294	287	293	289
Lamb-Mössbauer factor from *S*	0.6806 ± 0.0056	0.7251 ± 0.0031	0.6704 ± 0.0047	0.7483 ± 0.0040	0.7117 ± 0.0060
Mean square displacement $<z^2>$ from *S* ($Å^2$)	0.00722 ± 0.00011	0.00603 ± 0.00006	0.00751 ± 0.00010	0.00544 ± 0.00007	0.00638 ± 0.00012
Internal energy/atom from *S* (meV)	27.43 ± 0.84	28.06 ± 0.71	28.51 ± 0.84	28.62 ± 0.76	27.99 ± 1.12
Kinetic energy/atom from *S* (meV)	13.72 ± 0.42	14.03 ± 0.36	14.25 ± 0.42	14.31 ± 0.38	13.99 ± 0.56
Force constant from *S* (N/m)	**110 ± 14** ($Fe^{3+}/\Sigma Fe = 0$)	**155 ± 11** ($Fe^{3+}/\Sigma Fe = 0.2$)	**188 ± 16** ($Fe^{3+}/\Sigma Fe = 0.32$)	**196 ± 12** ($Fe^{3+}/\Sigma Fe = 0.05$)	**149 ± 25** ($Fe^{3+}/\Sigma Fe = 0$)
$^{56}Fe/^{54}Fe$ β coefficients from *S*					
$1000\ \ln\beta = A_1/T^2 + A_2/T^4 + A_3/T^6$ (*T* in K)					
A_1	3.137E + 05 ± 4.019E + 04	4.398E + 05 ± 3.225E + 04	5.357E + 05 ± 4.439E + 04	5.571E + 05 ± 3.556E + 04	4.258E + 05 ± 7.193E + 04
A_2	−8.326E + 08 ± 3.532E + 08	−1.275E + 09 ± 3.695E + 08	−2.240E + 09 ± 4.244E + 08	−2.305E + 09 ± 3.297E + 08	−1.319E + 09 ± 8.842E + 08
A_3	6.792E + 12 ± 5.394E + 12	7.292E + 12 ± 7.533E + 12	1.863E + 13 ± 6.982E + 12	1.870E + 13 ± 5.368E + 12	1.119E + 13 ± 1.828E + 13
$1000\ \ln\beta = B_1 <F>/T^2 - B_2 <F>^2/T^4$ (*T* in K)					
B_1	2904	2904	2904	2904	2904
B_2	62,800	50,339	57,846	55,171	53,799
Parameters from *g*					
Lamb-Mössbauer factor from *g*	0.6796	0.7237	0.6683	0.7454	0.7099
Mean square displacement $<z^2>$ from *S* ($Å^2$)	0.00725	0.00607	0.00756	0.00552	0.00643
$d<z^2>/dT$ ($Å^2$/K)	2.28E-05	1.87E-05	2.36E-05	1.66E − 05	1.98E-05
Critical temperature (K)	822	1002	796	1127	947
Resilience (N/m)	60	74	59	83	70
Internal energy/atom from *g* (meV)	27.44	28.06	28.52	28.63	27.99
Kinetic energy/atom from *g* (meV)	13.72	14.03	14.26	14.31	14.00
Vibrational entropy (kb/atom)	1.34	1.18	1.16	1.12	1.20
Helmholtz free energy (meV)	−7.12	−2.50	−1.55	−0.22	−3.09
Vibrational specific heat (kb/atom)	0.94	0.92	0.91	0.90	0.92
lamb-Mössbauer factor at T = 0 from *g*	0.90	0.91	0.91	0.91	0.91
Kinetic energy/atom at T = 0 from *g* (meV)	5.13	6.12	6.54	6.74	6.00
Force constant from *g* (N/m)	110	155	188	196	149

(*continued on next page*)

Table 3 (*continued*)

	Almandine (Garnet Hill, Ely, Nevada)	Ilmenite (NMNH96189)	Annite (M9297, Rockfort, Massachusetts)	Schorl (Erongo Region, Namibia)	Fayalite (M7652, Rockport, Massachusetts)
$^{56}Fe/^{54}Fe$ β coefficients from *g*					
$1000\ln\beta = A_1/T^2 + A_2/T^4 + A_3/T^6$ (T in K)					
A_1	3.143E + 05	4.403E + 05	5.383E + 05	5.593E + 05	4.26E + 05
A_2	−8.483E + 08	−1.287E + 09	−2.330E + 09	−2.39E + 09	−1.33E + 09
A_3	7.559E + 12	7.888E + 12	2.332E + 13	2.320E + 13	1.18E + 13
Velocities from *g*					
Input density (g/cc)	3.5	3.5	3.5	3.5	3.5
Input bulk modulus (GPa)	100	100	100	100	100
Debye velocity (m/s)	4887 ± 255	4095 ± 117	2915 ± 90	4522 ± 66	4058 ± 44
p-wave velocity (m/s)	7388 ± 189	6820 ± 78	6118 ± 51	7117 ± 47	6795 ± 29
s-wave velocity (m/s)	4416 ± 242	3668 ± 112	2578 ± 86	4070 ± 63	3633 ± 42
Poisson ratio	0.222	0.297	0.392	0.257	0.300

a Density Functional Theory (DFT) *ab initio* approach, assuming that iron only exists as Fe^{2+}. Due to the magnetic feature of Fe and relatively large sizes of the primitive cells of these minerals, it was challenging to compute their full vibrational spectra. Specifically, we frequently ran into divergence problems when we tried to compute the full vibrational spectra of these minerals. Therefore, we used the high-temperature approximation above (Eq. (5)) that relates the reduced partition function ratio to the mean force constant, and calculated the latter by displacing the iron atoms along three orthogonal directions in Cartesian coordinates. This is an approximate approach, and the full vibrational spectra were not obtained. This method has been successfully applied to several isotopic systems (*e.g.*, Kowalski and Jahn, 2011; Kowalski et al., 2013; Ducher et al., 2016). While more work will be needed to fully validate the force constants determined with this approach, we show below that their scaling with interatomic distances follows the trends defined by other minerals for which the full PDOS was measured or calculated, so we have no obvious reason to question this first-order approach.

If the element was located at more than one equivalent site, a weighted average was calculated based on the number of distinct sites. This was the case for fayalite, which has two Fe sites with equal numbers. Therefore, two force constants, one for each site, were calculated and their average (50:50 here) was calculated to give the fayalite force constant. The force constant in a specific direction was calculated following these steps: (*i*) the lattice parameters and atomic positions were relaxed starting from the experimentally determined structures; (*ii*) the atom of interest (Fe) was moved from its equilibrium position along x or y or z direction while keeping lattice and positions of other atoms constant; and (*iii*) the total energy was fitted against displacement using the formula for a harmonic potential ($\langle F\rangle$ is the effective force constant, x is the displacement from the equilibrium position),

$$E = \frac{1}{2}\langle F\rangle x^2 + \text{constant}. \tag{7}$$

The calculation of ground state potential energy surface was conducted by Quantum ESPRESSO (Giannozzi et al., 2009, 2017) with Perdew–Burke–Ernzerhof (PBE) generalized gradient approximation (GGA) (Perdew et al., 1996) and GBRV ultrasoft pseudopotentials (Garrity et al., 2014). For all systems, unless otherwise specified, a displacement step of 0.0025 Å and a uniform (Monkhorst-Pack) $2 \times 2 \times 2$ ($4 \times 2 \times 4$ for fayalite, $3 \times 3 \times 3$ for ilmenite) k-point mesh were used (Monkhorst and Pack, 1976). The cutoff energy of wave functions was set at 60 eV, so that the total energy converged within 5 meV/atom. The cutoff energy of charge density was set to 720 eV (dual of 12) as suggested in the literature (Lejaeghere et al., 2016; Prandini et al., 2018).

The structural configurations of the minerals can be found in the Supplementary Materials. The ilmenite, almandine and fayalite primitive cells were adopted from literature without modification (Hazen, 1977; Geiger et al., 1992; Yamanaka et al., 2007). The annite primitive cell was adopted from Redhammer et al. (2000) and a

$1 \times 1 \times 2$ supercell was built to accommodate its antiferromagnetic property (Rancourt et al., 1994). The schorl structure was adopted from Bačík et al. (2012), while replacing Na with Ca to balance charge, assuming 100% occupancy of O at position (0, 0, 0.7716), and a $2 \times 1 \times 1$ supercell was built to model antiferromagnetism. Cell parameters and the calculated Fe force constants of the minerals are compiled in Table 4.

2.4. Determination of Fe redox state using conventional Mössbauer spectroscopy

Iron redox state in minerals can affect equilibrium Fe isotope fractionation factors because Fe^{3+} tends to preferentially incorporate heavy Fe isotopes. Iron redox ratios of minerals from Moosilakue and minerals measured by NRIXS were therefore measured using conventional Mössbauer spectroscopy at the Argonne National Laboratory. The minerals were ground to fine powders to make mounts with an effective thickness of ~5 mg Fe/cm^2. This corresponds to ~30 mg mineral mass/cm^2 for tourmaline and ~15 mg mineral mass/cm^2 for other minerals. The sample area of the mounts was adjusted according to the available mass of each mineral (*i.e.*, if the powder mass is limited, the sample area has to be reduced in order to obtain the correct effective thickness), and final sample areas range from 0.04 to 1 cm^2 for spectra collection. All Mössbauer absorption spectra were collected at room temperature, with a measurement time of one to two days per mineral. Results were calibrated against an α-Fe foil of 25 μm thickness and 100% purity. The spectra were fit with doublets (Fig. 4) using a commercial software WinNormos (provided by WissEl company). The relative Fe^{2+} and Fe^{3+} proportions were derived from the relative areas of the doublets (Fig. 4; see Supplementary Table S4 for information on the assigned Fe redox states and relative areas). While the fitting parameters of Mössbauer spectra with doublets are non-unique, determining Fe redox states with Mössbauer spectroscopy is relatively straightforward, and different fit methods give consistent results. In this work the numbers of doublets to fit the spectra of the minerals were the same as those used in literature (Gibb et al., 1969; Annersten, 1974; Amthauer et al., 1976; Dyar and Burns, 1986; Ferrow et al., 1988; Virgo et al., 1988; Dyar et al., 1998).

3. RESULTS

3.1. Iron, Mg and Ti isotopic compositions of minerals from Mt. Moosilauke

The Fe isotopic compositions of mineral separates from the pelitic schist R71-90 from Mt. Moosilauke are reported in Table 1 and Fig. 2. The chemical compositions of the minerals can be found in Hodges and Spear (1982). To assess the reproducibility of the isotope measurements, we repeated the whole procedure, starting with mineral separation. The two groups of minerals separated from two rock chips of R71-90 (mineral separates 1 and 2 in Table 1 and Fig. 2) were measured for their Fe isotopic compositions. The expectation was that if the mineral separation was good, the two groups of minerals should give consistent Fe isotopic compositions. As shown in Fig. 2, garnet, ilmenite, biotite, tourmaline from the two groups show the same Fe isotopic compositions. Muscovite from the two groups show the same Fe isotopic composition within error but the errors are relatively large due to their low Fe contents. Plagioclase from the two groups are less consistent; this could be because plagioclase contains an extremely small amount of Fe, so isotopic compositions may be affected by the presence of a tiny amount of impurities in the plagioclase fractions.

The bulk rock of R71-90 has an Fe isotopic composition of $\delta^{56}Fe = +0.10 \pm 0.02‰$. The $\delta^{56}Fe$ values of the minerals vary significantly, from −0.22‰ to +0.40‰. Biotite has the same $\delta^{56}Fe$ value ($+0.10 \pm 0.02‰$; weighted average of mineral separates 1 and 2) as the bulk, which is expected because the rock is a pelitic schist and biotite dominates the Fe budget. Garnet and ilmenite have lighter Fe isotopic compositions of $-0.22 \pm 0.02‰$ and $-0.17 \pm 0.02‰$ respectively, while tourmaline, muscovite and plagioclase have heavier isotopic compositions. The weighted average of Fe isotopic compositions of tourmaline from the two mineral separates is $+0.20 \pm 0.02‰$. Muscovite and plagioclase are heavier than all other minerals, a weighted average of the two groups of mineral separates yielded $\delta^{56}Fe$ values for muscovite and plagioclase of $+0.34 \pm 0.02$ and $+0.28 \pm 0.05‰$, respectively. Quartz in mineral separate 1 was also measured for Fe isotopes. Quartz with two different colors (colorless and yellowish) were measured separately, and $\delta^{56}Fe$ values of $+0.40 \pm 0.04$ and $+0.27 \pm 0.04‰$ were obtained for colorless quartz and yellowish quartz respectively. Given the extremely low Fe content in quartz, these signatures are not representative of quartz itself but rather reflect the compositions of impurities or weathering products.

Large Mg isotopic variation was also observed in Moosilauke minerals (Table 2 and Fig. 3). The bulk rock has a $\delta^{26}Mg$ value of $-0.13 \pm 0.04‰$. Biotite has a $\delta^{26}Mg$ value of $-0.15 \pm 0.05‰$, the same as the bulk composition within error. Garnet and tourmaline have $\delta^{26}Mg$ values of -1.54 ± 0.07 and $+0.26 \pm 0.05‰$, respectively.

Ilmenite, biotite, and bulk were measured for Ti isotopic compositions (Table 2). Ilmenite has a Ti isotopic composition of $\delta^{49}Ti = +0.05 \pm 0.01‰$, lighter than the Ti isotopic composition of biotite and the bulk rock, which are $+0.43 \pm 0.01$ and $+0.23 \pm 0.02‰$, respectively.

3.2. Iron force constants from NRIXS measurements

The mineral thermo-elastic properties, including the mean force constants of the iron bonds, derived from NRIXS measurements of phonon excitation probability density $S(E)$ or the partial phonon density of states PDOS $g(E)$ are summarized in Table 3. We focus our discussion on the force constant as it is the dominant driver of equilibrium isotopic fractionation, especially at high temperature, but we also provide the 3rd order polynomial expansion in $1/T^2$ to calculate 1000 lnβ at any temperature (Table 3). The PDOS of the measured minerals can be found in the Supplementary Materials. The force constants are 110

Table 4
Iron force constants of minerals calculated by *ab initio* DFT approach.

	Almandine			Ilmenite			Annite			Schorl			Fayalite		
	Ab initio	Exper.	Diff.	*Ab initio*	Exper.	Diff.	*Ab initio*	Exper.	Diff.	*Ab initio*	Exper.	Diff.	Ab initio	Exper.	Diff.
a(Å)	10.069	9.981	0.89%	5.472	5.540	−1.22%	5.329	5.390	−1.14%	19.164	19.041	0.65%	4.856	4.818	0.78%
b(Å)	10.069	9.981	0.89%	5.472	5.540	−1.22%	5.331	5.390	−1.09%	9.581	9.520	0.64%	10.567	10.470	0.93%
c(Å)	10.069	9.981	0.89%	5.472	5.540	−1.23%	21.036	20.617	2.03%	9.581	9.520	0.64%	6.060	6.086	−0.43%
alpha	109.4	109.5	−0.07%	56.0	54.7	2.37%	94.7	95.1	−0.43%	113.9	113.8	0.10%	90.0	90.0	0.00%
beta	109.4	109.5	−0.07%	56.0	54.7	2.34%	94.8	95.1	−0.27%	113.9	113.8	0.09%	90.0	90.0	0.00%
gamma	109.4	109.5	−0.07%	56.0	54.7	2.36%	120.0	120.0	0.00%	113.9	113.8	0.09%	90.0	90.0	0.00%
<F>	**120**			**133**			**207**			**209**			**144**		

Exper.: experimentally measured lattice parameters. Diff.: difference between experimentally measured lattice parameters and calculated parameters. Experimentally measured lattice parameters are from literature (see main text). < F > is force constant in N/m.

± 14 N/m for almandine garnet (Garnet Hill, Ely Nevada), 155 ± 11 N/m for ilmenite (NMNH96189), 188 ± 16 N/m for annite (the Fe-rich endmember of the biotite solid solution; M9297; from Rockport, Massachusetts), 196 ± 12 N/m for schorl tourmaline (from Erongo Region, Namibia), and 149 ± 25 N/m for fayalite (M7652; from Rockport, Massachusetts). A synthetic ilmenite was measured before using NRIXS by Williams et al. (2016). They obtained a force constant of 156 ± 10 N/m, which is in excellent agreement with our measured value of 155 ± 11 N/m.

3.3. Iron force constants from *ab initio* calculations

The calculated mineral lattice parameters and force constants from the *ab initio* DFT approach are given in Table 4. Force constants are 120, 133, 207, 209 and 144 N/m for almandine, ilmenite, annite, schorl, and fayalite respectively. The result in general agrees with the NRIXS result (Table 3) of increasing force constants of almandine, ilmenite (similar to fayalite), annite, and schorl, and is also consistent with increasing δ^{56}Fe values of garnet, ilmenite, biotite and tourmaline in Moosilauke R71-90 (Table 1 and Fig. 2). The only exception is annite, for which *ab initio* yields a force constant that is slightly higher than that measured by NRIXS.

To assess the reliability of the calculated/measured force constants in this study, we further compare them with the force constants measured or computed in the literature. The expectation is that, to first order, Fe force constants should correlate with the Fe-O bond lengths in minerals where Fe is coordinated with O. The ionic bond model of Young et al. (2015) predicts that Fe force constants should correlate linearly with $1/r^3$, where r is the equilibrium Fe-O interionic distance. In Fig. 5, we therefore compare our measured/calculated Fe force constants with literature values in a plot $\langle F \rangle$ *vs.* $1/r^3$ (Table 5). Given that the Fe coordination in minerals affects Fe isotopic fractionation, we split minerals into 4-fold coordinated minerals and minerals with higher Fe coordinations. Not much data is available on 4-fold coordinated minerals, but a clear trend can be seen for minerals with Fe in 6-fold coordination. The force constants calculated in this study follow the trend defined by literature data.

Based on the agreement between force constant determinations based on NRIXS and *ab initio* calculations, and the similar relationship with interatomic distances as literature values, we believe that our force constant estimates are reliable. The displacement method is however limited, as it does not allow comparison with PDOS measured by NRIXS or other spectroscopic data, and further work will be needed to fully validate this approach.

3.4. Redox states of Fe in the minerals

Iron redox states were determined for both Moosilauke minerals and minerals used for NRIXS measurements (Fig. 4 and Table 6). Using electron microprobe data to calculate Fe redox state of ilmenite is fairly straightforward

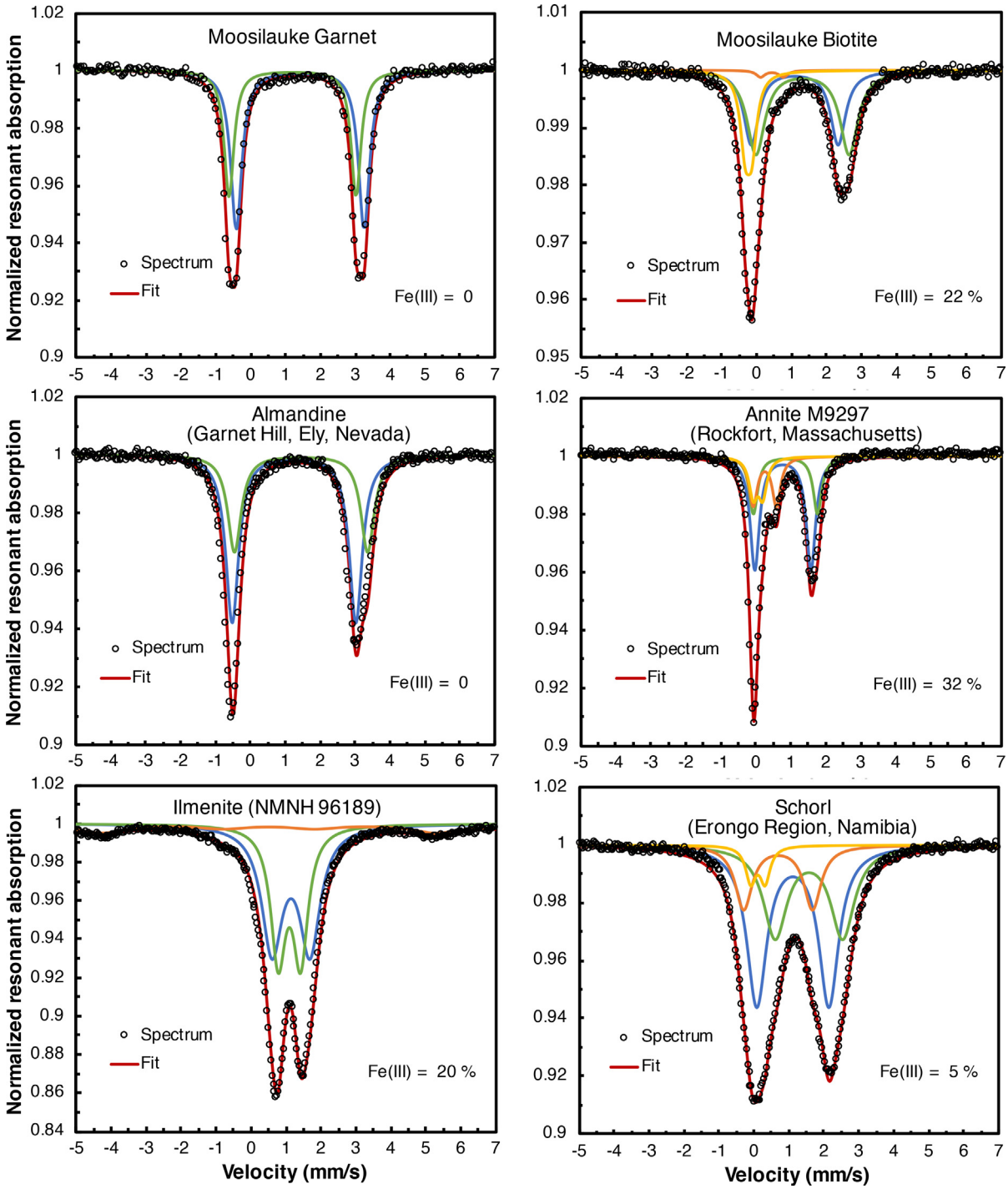

Fig. 4. Iron-57 Mössbauer spectra of the minerals studied.

and reliable (Droop, 1987). We calculated a $Fe^{3+}/\Sigma Fe$ ratio of ~0 for Moosilauke ilmenite based on its chemical composition determined with an electron microprobe. For minerals such as mica and tourmaline that contain vacant cation sites, the Fe redox states cannot be calculated from electron probe data with great confidence. In those cases, conventional Mössbauer spectroscopy was used to obtain the $Fe^{3+}/\Sigma Fe$ ratios. Moosilauke garnet and biotite have $Fe^{3+}/\Sigma Fe$ ratios of ~0 and 0.22, respectively. The minerals used specifically for NRIXS measurements were measured by Mössbauer and we found $Fe^{3+}/\Sigma Fe$ ratios for almandine (Garnet Hill), ilmenite (NMNH96189), annite (M9297), and schorl (Erongo Region, Namibia) of 0, 0.2, 0.32 and 0.05, respectively.

4. DISCUSSION

At the temperature of 400 °C or higher, Dauphas et al. (2012) showed that for iron, truncating the 1000lnβ polynomial expansion to the first order term $2904\langle F\rangle/T^2$ approximates the true value within 1% for force constant values less than 200 N/m that are relevant to the minerals studied here. We can therefore discuss equilibrium fractionation factor by focusing on the force constant. In the following, we first compare the force constants of minerals obtained using NRIXS and *ab initio* approaches. The force constants are used to derive equilibrium Fe isotope fractionation factors between minerals, which we then compare with Fe isotopic compositions of Moosilauke minerals. This allows us to assess whether Moosilauke minerals have reached isotopic equilibrium and whether the three methods are consistent. As shown below, Moosilauke minerals are in Fe, Mg and Ti isotopic equilibrium, and their isotopic compositions provide precise constraints of equilibrium isotope fractionation factors.

4.1. Comparison between NRIXS, *ab initio* calculations, experimental data, and measurements of mineral separates from the Moosilauke metapelite

In general, there is a good agreement between *ab initio*-calculated and NRIXS-measured iron mean force constants (Fig. 6 and Table 7). Both *ab initio* and NRIXS approaches give access to the reduced partition function ratios or β-factors (1000lnβ (^{56}Fe /^{54}Fe) $\simeq 2904\frac{\langle F\rangle}{T^2}$ at high temperature; Dauphas et al., 2012; Table 7), which correspond to equilibrium isotopic fractionations between the minerals and monoatomic gas of the element under consideration (Schauble, 2004; Blanchard et al., 2017). To compare these *ab initio* and NRIXS results with natural minerals from Mt. Moosilauke, we need to compare isotopic fractionation factors between minerals (Eq. (6)). Therefore, we plot the isotopic fractionation factors between mineral-garnet (almandine) pairs (Fig. 7 and Table 8). **Garnet (almandine)** is used as the normalization mineral because it shows great consistency among the three methods. Both the Moosilauke garnet and the almandine used for NRIXS measurements contain no Fe^{3+}, so a correction for Fe^{3+} for this mineral is not required, and a good agreement was found for the force constant of almandine between *ab initio* (120 N/m) and NRIXS (110 ± 14 N/m). Another virtue of comparing other minerals with garnet is that it has the lightest Fe isotopic composition and the lowest force constant, so the isotopic fractionations between minerals and garnet are always positive. In the following discussion, mineral-garnet isotope fractionations between Moosilauke minerals are calculated using their δ values ($\Delta_{mineral-garnet} = \delta_{mineral} - \delta_{garnet}$). For NRIXS and *ab initio* calculations, $\Delta^{56}Fe_{mineral-garnet}$ is calculated using their force constants:

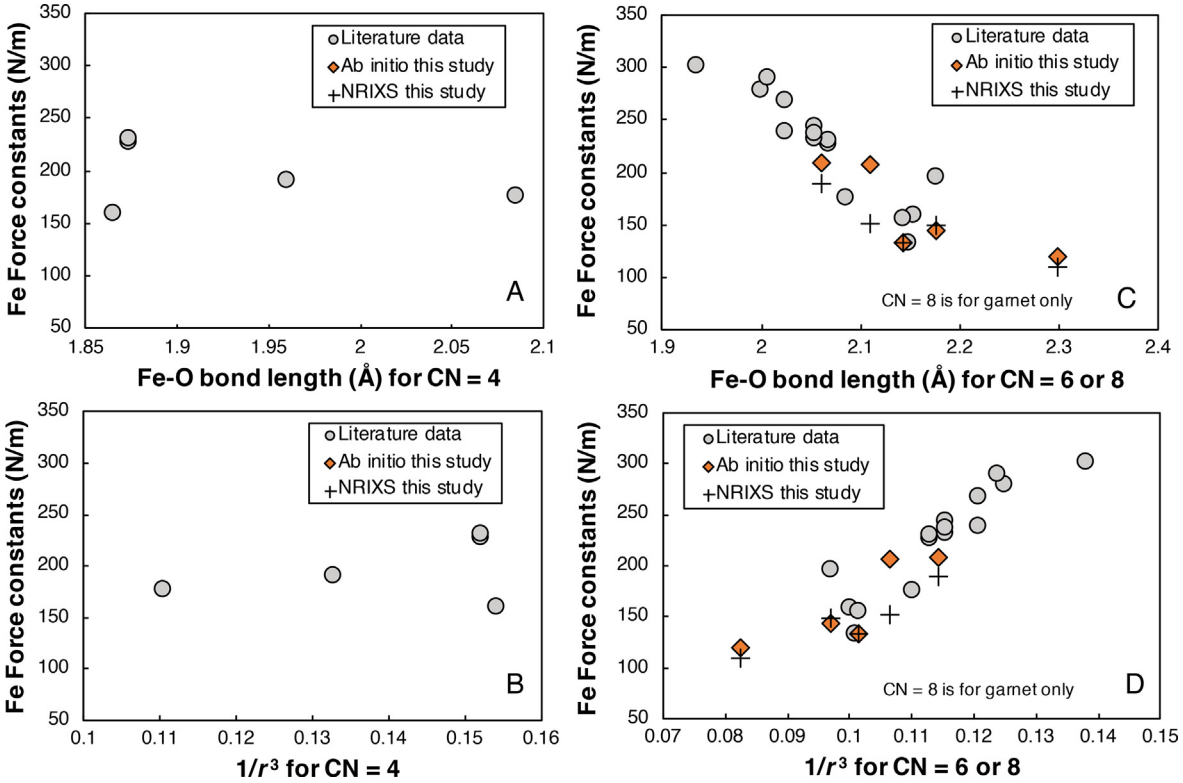

Fig. 5. Iron force constants (calculated by DFT or measured by NRIXS) vs. the Fe-O bond lengths of minerals. Minerals are plotted separately for 4-fold coordination (A and B) and higher coordinations (C and D). (A) and (C) show Fe force constants vs. Fe-O bond lengths, and (B) and (D) show Fe force constants vs. $1/r^3$, where r represents Fe-O bond lengths. Grey dots are literature data (see Table 5) and orange diamonds and black crosses are data from this study. The fact that the data from this study fall on the general correlation implies that our *ab initio* calculated and NRIXS measured force constants are reliable.

Table 5
Iron force constants and Fe-O bond lengths of minerals.

Phases	Method	<F> (N/m)	Note	Ref. for < F>	CN 1	Bond length (Å)	CN 2	Bond length (Å)	Ref. for CN
Magnetite	NRIXS	228	*	[1]	6	2.068	4	1.873	[10]
FeO (Wüstite)	NRIXS	160	*	[1]	6	2.153	4	1.865	[11]
Magnetite	NRIXS	230	*	[2]	6	2.068	4	1.873	[10]
Orthoenstatite	NRIXS	177	*	[2]	6	2.086	4	2.085	[12]
Hematite	NRIXS	244	*	[2]	6	2.054			[13]
Goethite	NRIXS	268	*	[3]	6	2.023			[14]
H-Jarosite	NRIXS	280	*	[3]	6	2.000			[15]
K-Jarosite	NRIXS	290	*	[3]	6	2.006			[16]
Olivine	NRIXS	197	*	[4]	6	2.176			[10]
Fe^{2+} in MgFeAl spinel	NRIXS	190	*	[5]			4	1.960	[17]
Fe^{3+} in MgFeAl spinel	NRIXS	302	*	[5]	6	1.934			[17]
Ilmenite	NRIXS	156	*	[6]	6	2.143			[10]
Hematite	*ab initio*	232	*	[7]	6	2.054			[18]
Siderite	*ab initio*	134	*	[7]	6	2.147			[19]
Goethite	*ab initio*	239	*	[3]	6	2.023			[20]
Hematite	*ab initio*	238	*	[8]	6	2.054			[13]
Almandine	*ab initio*	120	$	[9]	8	2.298			[10]
Ilmenite	*ab initio*	133	$	[9]	6	2.143			[10]
Annite	*ab initio*	207	$	[9]	6	2.109			[21]
Schorl	*ab initio*	209	$	[9]	6	2.060			[22]
Fayalite	*ab initio*	144	$	[9]	6	2.176			[10]
Almandine	NRIXS	110		[9]	8	2.298			[10]
Ilmenite	NRIXS	133	#	[9]	6	2.143			[10]
Annite	NRIXS	152	#	[9]	6	2.109			[21]
Schorl	NRIXS	190	#	[9]	6	2.060			[22]
Fayalite	NRIXS	149		[9]	6	2.176			[10]

CN: Coordination number. * Calculated using the beta factors reported in Dauphas et al. (2017). $ calculated using the displacement approach. # Fe^{3+} was corrected. [1] Polyakov et al. (2007). [2] Dauphas et al. (2012). [3] Blanchard et al. (2015). [4] Dauphas et al. (2014). [5] Roskosz et al. (2015). [6] Williams et al. (2016). [7] Blanchard et al. (2009). [8] Rustad and Dixon (2009). [9] This study. [10] Sossi and O'Neill (2017). [11] Fjellvåg et al. (1996). [12] Domeneghetti et al. (1995). [13] Maslen et al. (1994). [14] Alvarez et al. (2008). [15] Basciano and Peterson (2007). [16] Mills et al. (2013). [17] Lavina et al. (2009). [18] Maslen et al. (1994). [19] Lavina et al. (2010). [20] Alvarez et al.(2008). [21] Redhammer et al. (2000). [22] Fortier and Donnay (1975).

Table 6
Iron redox ratios determined using Mössbauer spectroscopy.

Minerals	$Fe^{3+}/\Sigma Fe$	Comments
Moosilauke minerals		
Garnet	0	Almandine; contains some Mn and Mg; Fe/(Fe + Mg + Mn) = 0.75[b]
Ilmenite	0[a]	Small amount of Mn; Fe/(Fe + Mn) = 0.95
Biotite	0.22	Fe/(Fe + Mg) = 0.5[b]
Tourmaline	n.d.	Fe/(Fe + Mg) = 0.35
Muscovite	n.d.	Fe/(Fe + Mg) = 0.46[b]
Plagioclase	n.d.	Albite[b]
Quartz	n.d.	
Minerals for NRIXS measurement		
Almandine (Garnet Hill, Ely Nevada)	0	Small amount of Mn and little Mg; Fe/(Fe + Mn) = 0.75
Ilmenite (NMNH96189)	0.20	Small amount of Mn and little Mg; Fe/(Fe + Mn) = 0.91
Annite (M9297)	0.32	Small amount of Mn and little Mg; Fe/(Fe + Mn) = 0.98
Schorl (Erongo Region, Namibia)	0.05	Fe-endmember of tourmaline; little Mn or Mg
Fayalite (M7652)	0	Small amount of Mn and little Mg; Fe/(Fe + Mn) = 0.97

a. calculated based on the chemical composition. b. from Hodges and Spear (1982); n.d. not determined. The ratios in the table are atomic ratios.

$\Delta^{56}Fe_{mineral-garnet} = 2904\frac{\langle F\rangle_{mineral}-\langle F\rangle_{garnet}}{T^2}$, where T is the temperature in K. The calculated fractionation factors between minerals and garnet as a function of temperature in the form of $\Delta^{56}Fe_{mineral-garnet} = A \times 10^6/T^2$ are summarized in Table 8.

For **ilmenite**, *ab initio* yields a value of 133 N/m, which is slightly lower than the NRIXS-measured force constant for ilmenite NMNH96189 of 155 ± 11 N/m. A synthetic ilmenite was measured previously by NRIXS and an almost identical value of 156 ± 10 N/m was obtained (Williams et al., 2016). The slightly higher NRIXS-measured force constant of ilmenite relative to the *ab initio* value could be due to the presence of Fe^{3+} in the ilmenite. The NMNH96189 ilmenite is a reference standard for electron microprobe analysis and has a well constrained $Fe^{3+}/\Sigma Fe$ ratio of 0.2 (Jarosewich et al., 1980), and this ratio is also confirmed by our Mössbauer analysis (Fig. 4 and Table 6). It has been shown in previous studies that Fe oxidation states can affect Fe force constants significantly. For example, Roskosz et al. (2015) found a strong dependence of Fe force constant on $Fe^{3+}/\Sigma Fe$ ratio in spinel, and a transition from pure Fe^{2+} spinel to its Fe^{3+} counterpart causing the Fe force constant to increase by 104 ± 17 N/m. Similarly, the force constants are shifted upwards by 145 ± 27 N/m and 156 ± 32 N/m for rhyolite and basaltic glass, respectively, between the Fe^{2+} and Fe^{3+} endmembers (Dauphas et al., 2014). Ilmenite forms a solid solution with hematite, which previous NRIXS work showed had a force constant of 244 N/m (Sturhahn et al., 1999; Dauphas et al., 2012). Assuming that the Fe mean force constant in this solid solution scales linearly with the $Fe^{3+}/\Sigma Fe$ ratio, we can write for Fe in this solid solution,

$$\langle F\rangle_{\text{Ilmenite-Hematite}}(N/m) = 111\frac{Fe^{3+}}{\sum Fe} + 133, \quad (8)$$

$$\text{or } \langle F\rangle_{\text{Ilmenite-Hematite}}\left(\frac{N}{m}\right) = 244\frac{Fe^{3+}}{\sum Fe} + 133\left(1-\frac{Fe^{3+}}{\sum Fe}\right). \quad (9)$$

The coefficients in Eq. (9) correspond to the pure hematite and ilmenite mean Fe force constants. The one for hematite (244 N/m) is from previous NRIXS measure-

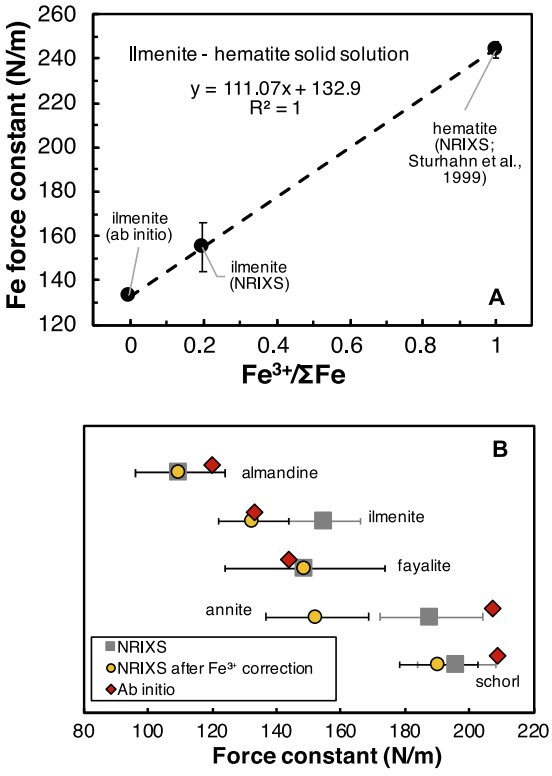

Fig. 6. Force constants derived from NRIXS and *ab initio* calculations. (A) Mean Fe force constant of ilmenite-hematite solid solution as a function of Fe^{3+} content. There is a 111 N/m difference between hematite and pure Fe^{2+} ilmenite. (B) Comparison of the force constants derived from the two approaches, before and after Fe^{3+} correction which assumes a 111 N/m difference between pure Fe^{3+} and Fe^{2+} endmembers as documented in ilmenite-hematite solid solutions. There is good agreement between the two approaches, except for annite.

Table 7
Comparison of mean Fe force constants and β-factors between *ab initio* calculations and NRIXS measurements.

Ab initio calculations				NRIXS				
Minerals	<F> (N/m)	1000 lnβ at 500 °C	1000 lnβ at 800 °C	Minerals	$Fe^{3+}/\Sigma Fe$	<F> (N/m) no Fe^{3+} correction	<F> (N/m) with Fe^{3+} correction	1000 lnβ at 500 °C	1000 lnβ at 800 °C
Almandine	120	0.58	0.30	Almandine (Ely, Nevada)	0	110 ± 14	110 ± 14	0.53 ± 0.07	0.28 ± 0.03
Ilmenite	133	0.65	0.34	Ilmenite (NMNH96189)	0.2	155 ± 11	133 ± 11	0.65 ± 0.05	0.34 ± 0.03
Annite	207	1.01	0.52	Annite M9297 (Rockfort, Massachusetts)	0.32	188 ± 16	152 ± 16	0.74 ± 0.08	0.38 ± 0.04
Schorl	209	1.02	0.53	Schorl (Erongo, Namibia)	0.05	196 ± 12	190 ± 12	0.92 ± 0.06	0.48 ± 0.03
Fayalite	144	0.70	0.36	Fayalite (M7652)	0	149 ± 25	149 ± 25	0.72 ± 0.12	0.38 ± 0.06

$1000\ ln\beta^{56/54}$ values were calculated using $1000\ ln\beta = 2904 < F > /T^2$. $Fe^{3+}/\Sigma Fe$ was determined using Mossbauer spectroscopy (Fig. 4 and Table 6). Fe^{3+} correction was done by assuming a 111 N/m difference between Fe^{3+} and Fe^{2+} mineral analogues.

ments (Sturhahn et al., 1999), while that for ilmenite (133 N/m) is from our *ab initio* DFT calculation performed for a $Fe^{3+}/\Sigma Fe$ ratio of 0 (Fig. 6A). The fact that our NRIXS measurements and *ab initio* calculations of ilmenite fall on a straight line with hematite (Fig. 6A) indicates that the main reason for the difference between the NRIXS and the *ab initio* results is the presence of Fe^{3+} in the former.

The ilmenite-garnet iron isotope fractionation has been previously determined in lab equilibration experiments at 800 °C (Sossi and O'Neill, 2017). This datum, as well as the fractionation measured in the Moosilauke samples, are evaluated against trends predicted by NRIXS and *ab initio* DFT predictions. In Fig. 7A we plot the isotopic fractionations between the ilmenite-garnet pair. We show the fractionations with their $Fe^{3+}/\Sigma Fe$ as measured, as well as the values corrected to the pure Fe^{2+} endmembers assuming a shift of 111 N/m between Fe^{2+} and Fe^{3+} counterparts (Eq. (8)). As shown, there is an overall excellent agreement between previous lab equilibration experiments (Sossi and O'Neill, 2017), Moosilauke minerals, NRIXS and *ab initio* approaches for the ilmenite-garnet pair. Our results point to an ilmenite and garnet (almandine) isotope fractionation, with only Fe^{2+} in the two minerals, of $\Delta^{56}Fe_{ilmenite-garnet} \simeq 0.05 \times 10^6/T^2$ (Table 8 and Fig. 7B).

This work provides the first estimate of Fe force constants for annite (the Fe-endmember of the biotite solid solution) and schorl (the Fe-endmember of tourmaline). For **annite (biotite)**, direct comparison of the force constants derived from *ab initio* calculations and NRIXS measurements reveals a small discrepancy (Fig. 6B and Table 7), with *ab initio* calculated value (207 N/m) higher than the NRIXS value (188 ± 16 N/m). However, as indicated by conventional Mössbauer, the NRIXS annite (M9297) contains about 32% Fe as Fe^{3+}. The force constant for the pure Fe^{2+} endmember is therefore predicted to be even smaller, thus increasing the discrepancy between NRIXS and *ab initio* results (Fig. 6 and Table 7). The Moosilauke biotite has 22% Fe^{3+}, and the biotite-garnet fractionation is consistent with NRIXS prediction both before and after Fe^{3+} correction (Fig. 7C and 7D). After correction for Fe^{3+} using the same method as for ilmenite-hematite solid solution (*i.e.*, assuming a 111 N/m difference between Fe^{3+} and Fe^{2+} endmembers), the two methods yielded the same isotope fractionation factor for Fe^{3+}-free endmembers of $\Delta^{56}Fe_{biotite-garnet} \simeq 0.12 \times 10^6/T^2$ (Table 8). Given the consistency between the NRIXS measurements and Moosilauke minerals, and the complexity of the crystal structure and primitive cell of annite in *ab initio* calculations, we suspect that *ab initio* (which gives a much larger fractionation) may suffer from a large error for annite. Ye et al. (2020) suggested an equilibrium Fe isotope fractionation factor of $\Delta^{56}Fe_{biotite-garnet} = 0.09(\pm 0.05) \times 10^6/T^2$ based on a pair of natural garnet and biotite that contain 5 and 29 % Fe^{3+} respectively. This fractionation factor, if corrected for Fe^{3+}, would correspond to a fractionation of $\sim 0.01(\pm 0.05) \times 10^6/T^2$, which is smaller than the fractionation factor constrained here. However, Fe isotopic fractionation in biotite and garnet may depend on their chemical compositions, which could explain the

observed discrepancy. Future work is needed to test how elemental compositions affect Fe isotope fractionation factors.

For **schorl (tourmaline)**, consistency among the three approaches was found. The NRIXS-measured force constant of 196 ± 12 N/m is within error of the *ab initio*-calculated value of 209 N/m (Table 7 and Fig. 6). For the mineral pair tourmaline-garnet, as shown in Fig. 7E and Table 8, the three methods all indicate a fractionation factor of $\Delta^{56}Fe_{tourmaline-garnet} = 0.25 \times 10^6/T^2$, before Fe^{3+} correction. The Fe^{3+} correction for NRIXS schorl (Erongo Region, Namibia) containing only 5% Fe^{3+} is minor. Moosilauke tourmaline was not measured for Fe^{3+} content due to the limited sample amount, but the consistency among the three methods may imply a minor Fe^{3+} content of Moosilauke tourmaline.

The Moosilauke sample does not contain any **olivine**. But a Mg-rich olivine (forsterite; Fo82) was measured previously using NRIXS by Dauphas et al. (2014), so here we measure an Fe-rich olivine (fayalite) using NRIXS for comparison. The mean Fe force constant of the fayalite measured by NRIXS is 149 ± 25 N/m. Electron microprobe analysis using EDS shows that this mineral contains little Mg (Fo = 0) and a minor amount of Mn (MnO = ~2 wt %; Table 6). This force constant is much lower than the value reported by Dauphas et al. (2014), who quoted an NRIXS-derived force constant of 197 ± 10 N/m for the forsterite (Fo = 82) they measured. The force constant of fayalite measured in this study is the same as the value derived from *ab initio* calculation (144 N/m) and from SOD shift (133 N/m; Polyakov and Mineev, 2000). Another evidence supporting low Fe force constant of fayalite is that it has a very similar value to ilmenite (155 ± 11 N/m), and previous lab equilibration experiments also showed little Fe isotopic fractionation between the two minerals (Sossi and O'Neill, 2017). The discrepancy between the force constants of forsterite and fayalite cannot be attributed to an error induced by different measurement sessions, because as shown above the NRIXS-derived force constants for ilmenite are identical from different sessions. Whether the discrepancy was caused by a difference in Mg content warrants further study. If it is true, this would translate to a mean Fe force constant for the forsterite-fayalite solid solution of

$$\langle F \rangle_{\text{Forsterite-Fayalite}}(N/m) = 0.59Mg^{\#} + 149 \quad (10)$$

where $Mg^{\#} = 100 \times Mg/(Mg + Fe)$.

In summary, after correction for variable Fe^{3+} contents in NRIXS-measured minerals and Mossilauke minerals, there is excellent agreement between the three approaches (Fig. 7 and Table 8). The only mineral that shows some discrepancy is biotite/annite (Fig. 7D). The measured isotopic fractionation between biotite and garnet in Moosilauke is consistent with NRIXS measurements but not with the *ab initio* calculations and we suspect that *ab initio* calculation may have suffered from a large error for annite. The consistency between the three approaches implies that Moosilauke minerals have reached Fe isotope equilibrium. Table 8 summarizes the equilibrium isotope fractionation factors determined in this study (all minerals are relative to garnet). We did not perform NRIXS or *ab initio* calculations for minerals with Fe in trace amounts (*e.g.*, muscovite and plagioclase), but their equilibrium isotope fractionation factors can be estimated using the Fe isotopic compositions of Moosilauke minerals, and they are also reported in Table 8.

4.2. Magnesium isotopic fractionations between Moosilauke minerals

The previous section shows that minerals from Mt. Moosilauke have reached Fe isotope equilibrium. Garnet, biotite and tourmaline have also been measured for their Mg isotopes, and whether the minerals reached Mg isotopic equilibrium needs to be assessed. As with Fe, we estimate that truncating the polynomial expansion to the first order (high-T limit) should yield accurate 1000 lnβ values within 1% for $^{26}Mg/^{24}Mg$ at 500 °C or higher. Magnesium does not contain Mössbauer isotopes, so its force constant cannot be measured using NRIXS. *Ab initio* calculations were not performed for Mg isotopes in this study, but literature data on *ab initio* calculations exist for some Mg-containing phases (Schauble, 2011; Huang et al., 2013; Wu et al., 2015). Given that Fe^{2+} and Mg^{2+} have similar ionic radii (0.78 *vs.* 0.72 Å) and often replace each other in the same crystal sites of minerals, one may expect them to show a correlation in their isotopic fractionations. In Table 9 and Fig. 8 we have compiled Mg *vs.* Fe isotope fractionations of minerals derived from *ab initio* calculations and NRIXS measurements (Polyakov and Mineev, 2000; Polyakov et al., 2007; Blanchard et al., 2009; Schauble, 2011; Dauphas et al., 2012; Huang et al., 2013; Roskosz et al., 2015). We find a trend for $\Delta^{26}Mg_{mineral-garnet}$ *vs.* $\Delta^{56}Fe_{mineral-garnet}$. The expected slope of the trend depends on Mg and Fe force constants and the masses of their isotopes,

$$\frac{\Delta^{Mg}_{A-B}}{\Delta^{Fe}_{A-B}} = \left(\frac{m^{26}-m^{24}}{m^{26}m^{24}}\right)\left(\frac{m^{56}m^{54}}{m^{56}-m^{54}}\right)\frac{\langle F\rangle^{Mg}_A - \langle F\rangle^{Mg}_B}{\langle F\rangle^{Fe}_A - \langle F\rangle^{Fe}_B} = 4.8\frac{\langle F\rangle^{Mg}_A - \langle F\rangle^{Mg}_B}{\langle F\rangle^{Fe}_A - \langle F\rangle^{Fe}_B} \quad (11)$$

If Fe and Mg have the same force constants in minerals, the slope should be 4.8 according to Eq. (11). However, most minerals plot slightly above the line (Fig. 8A). As pointed out by Schauble (2011), deviation from the simple mass-scaling relationship between Mg and Fe isotopes indicates that Mg forms slightly stiffer bonds than Fe. Regardless of the difference, equilibrium Mg *vs.* Fe fractionations of minerals show a trend in Fig. 8, and the Moosilauke minerals (tourmaline, biotite and garnet) follow this trend, suggesting that most likely Moosilauke minerals have reached Mg and Fe isotopic equilibrium.

Converting the Mg isotopic differences between Moosilauke minerals to the temperature-dependent form (*i.e.*, $\Delta^{26}Mg_{mineral-garnet} = A \times 10^6/T^2$; Fig. 8 and Table 8) gives a biotite-garnet equilibrium fractionation factor of $\Delta^{26}Mg_{biotite-garnet} = 0.83(\pm 0.05) \times 10^6/T^2$. This fractionation agrees with the equilibrium fractionation reported

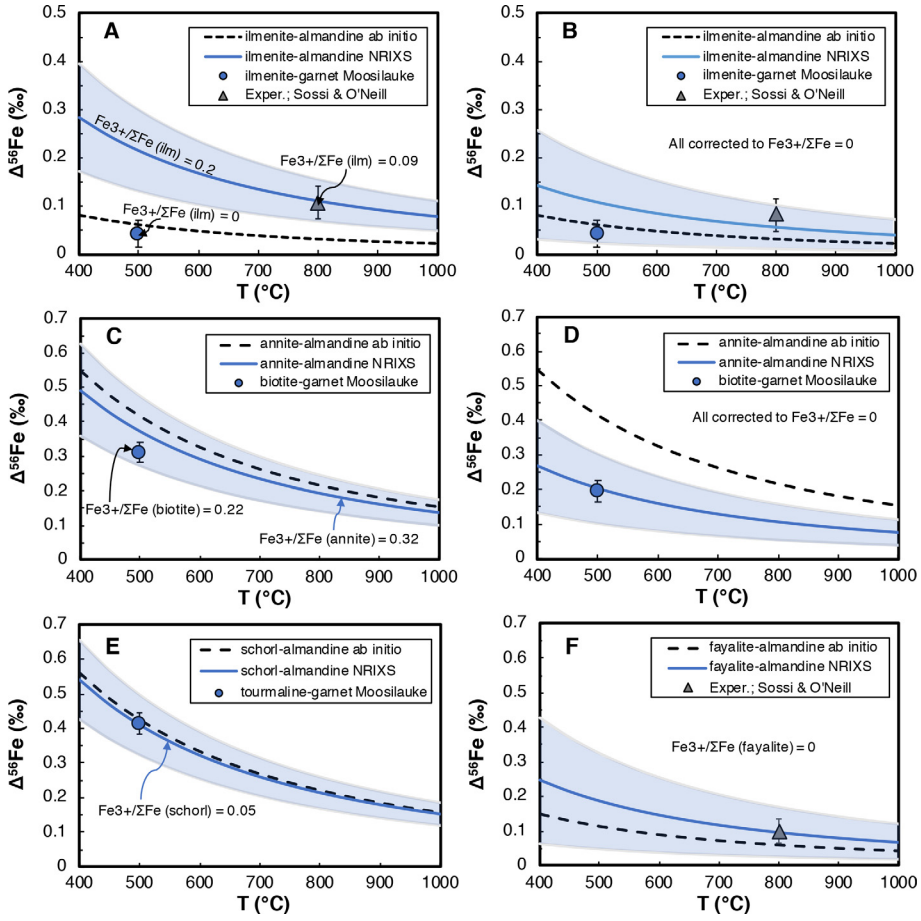

Fig. 7. Comparison between δ^{56}Fe analyses of Moosilauke minerals, NRIXS measurements, and *ab initio* calculations of Fe isotope fractionation between minerals. The blue shaded areas represent the errors of NRIXS measurements. Isotopic fractionations are expressed as isotopic differences between minerals and garnet (almandine). All iron in Moosilauke garnet and NRIXS-measured almandine is present as Fe^{2+}. Iron for *ab initio* calculations is assumed to be all Fe^{2+}. (A) Isotopic fractionation between ilmenite and garnet. Isotopic fractionation between Moosilauke ilmenite ($Fe^{3+}/\Sigma Fe = 0$) and garnet ($Fe^{3+}/\Sigma Fe = 0$) (filled blue circle; corresponds to $\Delta_{ilmenite\text{-}garnet} = 0.03(\pm0.02) \times 10^6/T^2$) is consistent with that of *ab initio* calculations (black dash line; $\Delta_{ilmenite\text{-}almandine} = 0.04 \times 10^6/T^2$). NRIXS-measured fractionation (blue curve) and the fractionation determined by lab experiments (Sossi and O'Neill, 2017) are higher, but after correcting for Fe^{3+} in ilmenite measured here by NRIXS ($Fe^{3+}/\Sigma Fe = 0.2$) and studied by Sossi et al ($Fe^{3+}/\Sigma Fe = 0.09$) would bring the fractionations down to values that are consistent with Moosilauke minerals and *ab initio* calculations, as shown in (B). (B) Isotopic fractionation between ilmenite and garnet after correcting for Fe^{3+}, assuming a 111 N/m difference between Fe^{3+} and Fe^{2+} counterparts. (C) Isotopic fractionation between biotite and garnet. Isotopic compositions of Moosilauke biotite ($Fe^{3+}/\Sigma Fe = 0.22$) and garnet ($Fe^{3+}/\Sigma Fe = 0$) correspond to a fractionation of $\Delta_{biotite\text{-}garnet} = 0.19\ (\pm 0.02) \times 10^6/T^2$ (filled blue circle). NRIXS measurements (blue curve) yielded $\Delta_{annite\text{-}almandine} = 0.22(\pm0.06) \times 10^6/T^2$ with $Fe^{3+}/\Sigma Fe = 0.32$ for annite and $Fe^{3+}/\Sigma Fe = 0$ for almandine. The *ab initio*-calculated fractionation factor for the pure Fe^{2+} endmembers (black dash line) is $\Delta_{annite\text{-}almandine} = 0.25 \times 10^6/T^2$. (D) Isotopic fractionation between biotite and garnet after correcting for Fe^{3+} assuming a 111 N/m difference between pure Fe^{3+} and Fe^{2+} biotite. NRIXS measurements ($\Delta_{annite\text{-}almandine} = 0.12(\pm0.06) \times 10^6/T^2$ after correction for Fe^{3+}) and Moosilauke minerals ($\Delta_{biotite\text{-}garnet} = 0.12(\pm0.02) \times 10^6/T^2$ after correction for Fe^{3+}) show excellent consistency, while *ab initio* calculation gives a larger fractionation that may have suffered from a large error. (E) Isotopic fractionation between tourmaline and garnet. Great consistency among Moosilauke minerals, NRIXS measurements and *ab initio* calculations was found, pointing to a fractionation factor of $\Delta_{tourmaline\text{-}garnet} = 0.25(\pm0.02) \times 10^6/T^2$. $Fe^{3+}/\Sigma Fe$ was not measured for Moosilauke tourmaline due to the limited amount of the mineral, but tourmaline for NRIXS measurements had $Fe^{3+}/\Sigma Fe = 0.05$, a correction for Fe^{3+} is minor and would lead to a fractionation of $\Delta_{tourmaline\text{-}garnet} = 0.23(\pm0.02) \times 10^6/T^2$. (F) Isotopic fractionation between fayalite and garnet. Fayalite is not present in the Mossilauke sample, and NRIXS ($\Delta_{fayalite\text{-}almandine} = 0.11(\pm0.08) \times 10^6/T^2$; $Fe^{3+}/\Sigma Fe = 0$ for fayalite) and *ab initio* ($\Delta_{fayalite\text{-}almandine} = 0.07 \times 10^6/T^2$) results are shown, together with experimental data from Sossi and O'Neill (2017).

by Wang et al. (2015b), who found the relationship ~0.83–0.96 $\times 10^6/T^2$ based on isotopic compositions of natural minerals from metapelites, again implying that Mg isotopic equilibrium has been reached between Moosilauke biotite and garnet. Magnesium isotopic fractionation between tourmaline and garnet had not been previously constrained, and our study suggests an equilibrium isotope fractionation factor of $\Delta^{26}Mg_{tourmaline-garnet} = 1.08(\pm0.05) \times 10^6/T^2$. Wang et al. (2020b) measured Mg isotopic compositions of mineral separates from Himalayan leucogranites and found

Table 8
Iron and Mg isotope fractionations between minerals and garnet, and Ti isotope fractionation between biotite and ilmenite.

Methods	Ilmenite-Garnet	Biotite-Garnet	Tourmaline-Garnet	Fayalite-Garnet	Muscovite-Garnet	Plagioclase-Garnet
Fe isotope fractionation	**A value in $\Delta^{56/54}Fe = A \times 10^6/T^2$**					
Moosilauke minerals (before Fe^{3+} correction)	0.03 ± 0.02 ($Fe^{3+}/\Sigma Fe = 0$)	0.19 ± 0.02 ($Fe^{3+}/\Sigma Fe = 0.22$)	0.25 ± 0.02 ($Fe^{3+}/\Sigma Fe$ unknown)	–	0.33 ± 0.02 ($Fe^{3+}/\Sigma Fe$ unknown)	0.30 ± 0.03 ($Fe^{3+}/\Sigma Fe$ unknown)
Moosilauke minerals (Fe^{3+} content corrected to 0)	0.03 ± 0.02	0.12 ± 0.02	–	–	–	–
NRIXS (before Fe^{3+} correction)	0.13 ± 0.05 ($Fe^{3+}/\Sigma Fe = 0.2$)	0.22 ± 0.06 ($Fe^{3+}/\Sigma Fe = 0.32$)	0.25 ± 0.05 ($Fe^{3+}/\Sigma Fe = 0.05$)	0.11 ± 0.08 ($Fe^{3+}/\Sigma Fe = 0$)	–	–
NRIXS (Fe^{3+} content corrected to 0)	0.07 ± 0.05	0.12 ± 0.06	0.23 ± 0.05	0.11 ± 0.08	–	–
Ab initio calculations (Fe^{3+} content is 0)	0.04	0.25	0.25	0.07	–	–
Mg isotope fractionation	**A value in $\Delta^{26/24}Mg = A \times 10^6/T^2$**					
Moosilauke minerals	–	0.83 ± 0.05	1.08 ± 0.05	–	–	–
Ti isotope fractionation	**A value in $\Delta^{49/47}Ti = A \times 10^6/T^2$**					
Moosilauke minerals	0.23 ± 0.01 for Biotite-Ilmenite					

For Fe^{3+} correction, an isotopic difference of 111 N/m between Fe^{3+} and Fe^{2+} mineral endmembers was assumed. Garnet does not contain Fe^{3+}. The $Fe^{3+}/\Sigma Fe$ ratios in brackets are the ratios of the minerals that were compared to garnet.

an isotopic difference between tourmaline and garnet from 0.82 to 1.63‰, in general consistent with the large isotopic difference between the two minerals observed in this study.

4.3. Titanium isotopic fractionation between biotite and ilmenite

Moosilauke ilmenite, biotite, and the bulk rock were measured for their Ti isotopic compositions, with ilmenite ($+0.05 \pm 0.01$‰ for $\delta^{49/47}Ti$) being isotopically lighter than the bulk rock ($+0.23 \pm 0.02$‰) and biotite ($+0.43 \pm 0.01$‰). At 500 °C, the first order term of the polynomial expansion should yield $1000 \ln\beta$ values accurate within 1% for the $^{49}Ti/^{47}Ti$ ratio. Unlike Mg and Fe, the titanium isotopic composition of the bulk rock is not solely controlled by biotite ($TiO_2 = 1.3$ wt%; Hodges and Spear, 1982) but also by ilmenite. The Ti isotope fractionation between biotite and ilmenite is large, $+0.38 \pm 0.02$‰ at 500 °C, which corresponds to a temperature-dependent Ti isotope fractionation of $\Delta^{49}Ti_{biotite-garnet} = +0.23(\pm 0.01) \times 10^6/T^2$ (Table 8). In ilmenite, Ti is 6-fold coordinated. In biotite, there is some uncertainty as to how Ti^{4+} is present, but in all cases it involves Ti substituting for a lower charge cation in the octahedral layer (Henry and Guidotti, 2002; Henry et al., 2005), meaning that Ti in biotite should also be 6-fold coordinated. Therefore, similar oxidation state and coordination number of Ti are present in ilmenite and biotite, and it is difficult to explain the much heavier Ti isotopic composition of biotite relative to ilmenite with these two parameters. Wang et al. (2020a) calculated equilibrium Ti (either Ti^{3+} or Ti^{4+}) isotopic fractionations between various minerals using *ab initio* calculations. Although biotite was not included, they found significant variation in reduced partition function ratios of geikielite-ilmenite solid solutions (up to 0.45‰ at 500 °C), despite the fact that Ti is in same valence state of +4 and the same coordination number of 6, implying an effect of Fe/(Fe + Mg) ratio on Ti reduced partition function ratio. The finding of significant Ti isotopic fractionation between biotite and ilmenite is therefore not out of line with model predictions, but further work is needed to ascertain its origin.

5. APPLICATIONS

5.1. Iron and Mg isotopic fractionations during anatexis

Melting of the lower crust and the subsequent migration of the partial melt to the upper crust during orogenesis play a key role in the chemical differentiation of the continental crust (Rudnick and Gao, 2003; Brown and Rushmer, 2006), but the isotopic fractionation during the process has not been well constrained. Here we show that our newly constrained Fe and Mg isotope fractionation factors can be applied to modeling isotopic fractionation during this important process of intracrustal differentiation.

Fluid undersaturated melting likely predominates over fluid-saturated melting during high-grade metamorphism, and melt production usually involves the breakdown of hydrated minerals such as mica and amphibole

(*e.g.*, Yardley and Valley, 1997; Clemens, 2006). Muscovite/biotite dehydration melting is typical at ~750–900 °C and crustal pressures, and is commonly observed in orogens (*e.g.*, Clemens, 2006; Brown, 2013). The biotite breakdown reaction in high-grade metapelite (~825–900 °C) is the focus of the Fe and Mg isotope fractionation modelling presented below, because it yields relatively large quantity of melts compared to muscovite dehydration melting (Clemens and Vielzeuf, 1987; Vielzeuf and Holloway, 1988; Patiño and Johnston, 1991). According to Patiño and Johnston (1991), biotite reacts over a temperature interval of 825–975 °C at 10 kbar, with the melt fraction increasing steadily. The reaction was described as,

$$1\text{g Bt} + 0.55\text{g Pl} + 0.14\text{g Als} + 0.76\text{g Qz} = 1.72\text{g Melt} + 0.73\text{g Grt}. \quad (12)$$

(Bt: biotite; Pl: plagioclase; Als: aluminosilicates; Qz: quartz; Grt: garnet). In this reaction, biotite breaks down to produce melt and garnet that would be a residual refractory phase in the source during melt extraction. In order to model Fe and Mg isotopic fractionation in this reaction, we use the biotite-garnet Fe isotopic fractionation factors that we derived (Tables 8 and 10). The isotopic fractionation factors between the minerals and melt are unknown, but can be constrained using the NRIXS-derived Fe force constant of biotite (this study) and the force constant of rhyolite glass reported in Dauphas et al. (2014). The NRIXS-measured biotite ($Fe^{3+}/\Sigma Fe = 0.32$) has a force constant of 188 ± 16 N/m. Correction to a $Fe^{3+}/\Sigma Fe$ ratio of 0.22 (*i.e.*, the ratio in Moosilake biotite) would lead to a force constant of 176 N/m. Dauphas et al. (2014) found a correlation between the mean Fe force constant and the $Fe^{3+}/\Sigma Fe$ ratio in rhyolite glass. At a $Fe^{3+}/\Sigma Fe$ ratio of 0.22 similar to Moosilauke biotite (*i.e.*, assuming the melt and biotite have similar $Fe^{3+}/\Sigma Fe$ ratios), we estimate the mean Fe force constant to be 272 N/m. These values for biotite and rhyolite glass correspond to an equilibrium fractionation of +0.22‰ (*i.e.*, $\Delta^{56}Fe_{melt-bt} = 0.22‰$) at 850 °C. For Mg isotopic fractionation between melt and biotite, for lack of better constraints, we assume that $\Delta^{Mg}_{Melt-Bt} = 4.4\Delta^{Fe}_{Melt-Bt}$, as has been observed for equilibrium Fe and Mg isotopic fractionations between biotite and garnet (*i.e.*, $\Delta^{Mg}_{Bt-Grt} = 4.4\Delta^{Fe}_{Bt-Grt}$) in the Moosilauke minerals.

Based on the stoichiometry of the Eq. (12), each mole of Fe in biotite consumed would generate 0.75 moles of Fe in garnet and 0.25 moles of Fe in melt. Magnesium released from the breakdown of biotite would distribute among the three phases according to the Fe-Mg exchange coefficients (Table 10; Breton and Thompson, 1988). Biotite dominates the Fe and Mg budget in metapelites similar to Moosilauke metapelites, and its Mg and Fe isotopic compositions also represent the isotopic composition of bulk protolith prior to the dehydration melting. We are interested in the isotopic difference between melt and protolith, so the isotopic fractionation is expressed relative to the bulk original metapelite. The results of the model are shown in Fig. 9. In general, the melt has Fe and Mg isotopic compositions heavier than biotite and garnet. For Fe, the melt becomes progressively heavier for both batch equilibrium and Rayleigh distillation, reaching a melt-biotite (protolith) difference up to +0.3‰. For Mg, batch equilibrium would cause the isotopic composition of the melt to decrease slightly, but a Rayleigh distillation would lead to an increase in the isotopic composition of the melt reaching +1.2‰ (*i.e.*, 1.2‰ difference between melt and protolith). An important driver for the relatively large fractionations is the formation of isotopically light garnet in the residue. In summary, this three-phase fractionation model suggests that the granitic melt produced from biotite dehydration melting of metapelitic rocks during anatexis is isotopically heavier than the source, by ~0.2–0.3‰ for Fe isotopes and by ~0.9–1.2‰ for Mg isotopes, provided that equilibrium isotope fractionation prevails during partial melting and no melt exchange with surroundings. The spread of isotopic composition of the melt is relatively small, ~0.1‰ for Fe isotopes, and ~0.3‰ for Mg isotopes.

Our modeled results are in excellent agreement with a recent study by Telus et al. (2012), who studied the Fe, Mg, Zn, and U isotopic compositions of migmatites, granitoids, and pegmatites from the Black Hills, South Dakota that experienced a similar mica dehydration melting. Using the leucosomes in migmatites to represent granitic melt, the melanosome to represent the residue, and the nearby schist to represent the bulk source composition prior to the migmatization, they found a ~ +0.2‰ melt-source Fe isotopic fractionation. This is consistent with our modeled results suggesting that the melt should be isotopically heavier than the source by ~0.2–0.3‰. Furthermore, the limited isotopic variation of the melt in our model, ~0.1‰ variation for Fe isotopes, and ~0.3‰ variation for Mg isotopes, is in general consistent with the observed limited isotopic variations in S-type granites of ~0.15‰ and ~0.1‰ for Fe isotopes and Mg isotopes, respectively (Li et al., 2010; Telus et al., 2012). However, our model considered only the biotite dehydration reaction under equilibrium conditions. Other Fe-bearing phases in the source such as Fe oxides, if present, could modify the Fe isotopic compositions of the phases modeled here if there is any isotopic exchange between them during the process. Anatexis could also involve other processes such as assimilation and diffusion, which can induce further Fe and Mg isotopic variations in granites.

5.2. Heavy Fe isotopic composition of lunar ilmenite

Ilmenite is an important mineral in lunar petrogenesis. Two types of mare basalts that have been identified in the returned Apollo samples are low-Ti and high-Ti basalts. High-Ti basalts are distinguished from low-Ti basalts by their very high TiO_2 content (in excess of 6 wt%) and abundant (10–20 modal %) ilmenite (Papike et al., 1976). Previous petrological studies have shown that the two types of basalts cannot be related to each other by fractional crystallization, and melting of different source regions is required (Walker et al., 1975; Kesson and Ringwood, 1976). The formation of high-Ti basalts might have involved melting of a source region that include Fe- and Ti-rich oxides that were produced in the late stage of lunar magma ocean and were mixed subsequently with early

Table 9
Comparison of Mg and Fe isotope fractionation factors at 500 °C.

Minerals	1000lnβ $^{26/24}$ Mg at 500 °C	$\Delta^{26/24}$Mg (mineral-garnet)	Ref.	Minerals	1000 lnβ $^{56/54}$ Fe at 500 °C	$\Delta^{56/54}$Fe (mineral-garnet)	Ref.
Periclase	4.435	2.145	[1]	Wustite	0.760	0.240	[3]
Dolomite	3.503	1.213	[1]	Ankerite	0.475	−0.045	[4]
Magnesite	3.332	1.042	[1]	Siderite	0.630	0.110	[5]
Spinel	5.487	3.197	[1]	Spinel	0.900	0.380	[6]
Forsterite	3.898	1.608	[1,2]	Fayalite	0.710	0.190	[7]
Orthoenstatite	4.031	1.741	[1,2]	Orthoenstatite	0.840	0.320	[8]
Diopside	4.109	1.819	[1,2]	Diopside	0.935	0.415	[4]
Pyrope	2.290	0.000	[2]	Almandine	0.520	0.000	[7]

[1] Schauble, 2011. [2] Huang et al., 2013. [3] Polyakov et al., 2007. [4] Polyakov and Mineev, 2000. [5] Blanchard et al., 2009. [6] Roskosz et al., 2015; [7] This study. [8] Dauphas et al., 2012.

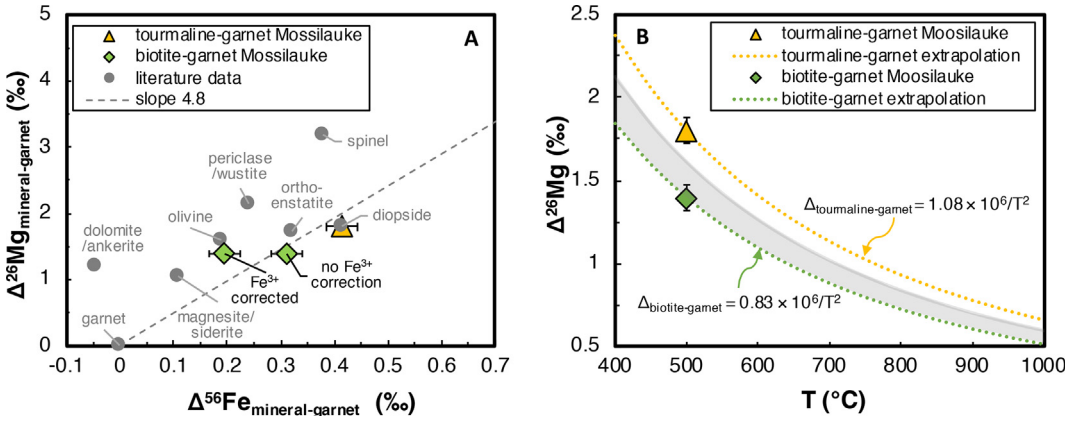

Fig. 8. Magnesium isotope fractionations between Moosilauke minerals, compared to literature data. (A) Magnesium isotopic fractionations vs. Fe isotopic fractionations for mineral-garnet pairs at 500 °C. Moosilauke minerals (colored symbols) are compared with minerals reported in literature (grey dots are literature data showing the equilibrium Mg and Fe isotope fractionations based on *ab initio* calculations and NRIXS measurements; see Table 9; Polyakov and Mineev, 2000; Polyakov et al., 2007; Blanchard et al., 2009; Schauble, 2011; Dauphas et al., 2012; Huang et al., 2013; Roskosz et al., 2015). Slope 4.8 line indicates the mass scaling relationship if Mg and Fe have the same bond strength in analogous minerals. Moosilauke minerals following the trend defined by literature minerals suggests that they have most likely reached Mg and Fe isotopic equilibrium. (B) Magnesium isotope fractionations of biotite-garnet and tourmaline-garnet pairs. Isotopic difference between biotite and garnet (green diamond) corresponds to a fractionation of $\Delta_{\text{biotite-garnet}} = 0.83(\pm0.05) \times 10^6/T^2$. This fractionation agrees with the fractionation of 0.83–0.96 × $10^6/T^2$ reported in Wang et al. (2015b) (shaded grey area). Magnesium isotopic fractionation between tourmaline and garnet as a function of temperature, calculated using the isotopic difference between the two minerals (yellow triangle) at 500 °C, is $\Delta_{\text{tourmaline-garnet}} = 1.08(\pm0.05) \times 10^6/T^2$.

mafic cumulates as a result of lunar mantle overturn (Kesson and Ringwood, 1976). The Mg and Fe isotopic compositions of the two types of basalts are clearly distinct, with high Ti basalts systematically shifted relative to low-Ti basalts by ~+0.1‰ for δ^{56}Fe (Poitrasson et al., 2004; Weyer et al., 2005; Craddock et al., 2010; Liu et al., 2010) and ~− 0.1‰ for δ^{26}Mg (Sedaghatpour et al., 2013). This isotopic difference between low-Ti and high-Ti mare basalts was likely set during lunar magma ocean (LMO) stage, reflecting signatures of LMO cumulates that later on were remelted to produce mare basalts (Sedaghatpour and Jacobsen, 2019). Comparison of low and high-Ti mare basalts thus suggests that ilmenite-rich cumulates in the LMO have heavy Fe isotopic composition relative to lunar mantle source regions not enriched in ilmenite.

Measurements of the mineral separates from low-Ti and high-Ti mare basalts also reveal that ilmenite in those basalts, on average, have heavier isotopic composition than the co-existing pyroxene and olivine (Craddock et al., 2010; Wang et al., 2015a). Based on mass balance, Craddock et al. (2010) suggested that the Fe isotopic composition of low-Ti basalts was controlled mainly by that of pyroxene while that of high-Ti basalts was controlled by ilmenite and pyroxene. The measured heavier Fe isotopic composition of ilmenite relative to pyroxene in mare basalts is at odds with the discussion above that under equilibrium conditions ilmenite should have lighter Fe isotopic composition compared to Mg-rich olivine and pyroxene (the force constant of pyroxene was not measured in this study but can be found in literature; Table 5).

Below, we examine whether the reason for the measured heavy Fe isotopic composition of (1) ilmenite mineral separates in mare basalts, and (2) bulk high-Ti mare basalts is that the signature was established during crystallization

of earlier phases. This is a difficult idea to test for the LMO as a whole, but we evaluate below whether this is a viable interpretation for minerals separated in mare basalts. We modelled the Fe isotopic evolution during the crystallization of melts with both low-Ti and high-Ti mare basalt compositions (see Supplementary Materials for details). The mineral crystallization sequences were calculated using the MELTS program, and equilibrium Fe isotope fractionation factors between phases as a function of temperature were calculated using the force constants constrained in this study and in the literature (Table S3). The results show that for both low-Ti and high-Ti starting compositions, the Fe isotopic composition of ilmenite (both instantaneously crystallized and bulk/cumulate) is never heavier than that of pyroxene or olivine (either instantaneously crystallized or bulk) during crystallization (Fig. 10). Therefore, equilibrium crystallization of minerals from mare basalt melts was unlikely to cause the observed heavier Fe isotopic composition of ilmenite relative to pyroxene/olivine.

Therefore, the heavy Fe isotopic composition of ilmenite mineral separates measured by Craddock et al. (2010) most likely reflects non-equilibrium conditions. One possible explanation for the heavy isotopic compositions of ilmenite in mare basalts is that it is controlled by Fe-Mg interdiffusion during crystallization of ilmenite. Large diffusion-driven Fe and Mg isotopic fractionations have been observed in terrestrial ilmenite (Tian et al., 2020). For ilmenite to acquire an elevated δ^{56}Fe through diffusion, Fe has to diffuse out of ilmenite while Mg diffuses in, which could happen if ilmenite interacted with a Mg-rich melt. However, during mineral crystallization one would expect the melt to become progressively Fe-rich and Mg-depleted. Tian et al. (2020) invoked a model of interstitial immiscible liquid phase segregation to explain the occurrence of a Mg-rich melt during ilmenite formation in a terrestrial setting. Diffusion-driven isotopic fractionation during the evolution of immiscible silica melts has also been invoked to explain the large Fe isotopic variations observed in A-type granitoids (Zhu et al., 2015). These processes, however, are not necessarily relevant to the melts that lunar ilmenite crystallized from. Measurements of Mg isotopes of lunar ilmenite and associated minerals are needed to further assess this possibility.

Another possibility for producing Fe isotopically heavy ilmenite in mare basalts is if ilmenite was derived from armalcolite $(Mg,Fe)Ti_2O_5$ initially crystallized from the melts of the mare basalt source region. In mare basalts, ilmenite has been observed to sometimes occur as mantles on armalcolite, indicating formation through either breakdown of armalcolite (into ilmenite and rutile) or reaction between armalcolite and basaltic liquid or other phases (El Goresy et al., 1974). Armalcolite has shorter Fe—O bonds than ilmenite (Wechsler et al., 1976; Wechsler and Prewitt, 1984), and could have heavier Fe isotopic composition than ilmenite during equilibrium crystallization. Inheriting Fe isotopic composition from armalcolite could thus have led to a heavy Fe isotopic composition in ilmenite. Further work on lunar ilmenite is needed to elucidate the origin of the heavy Fe isotopic composition of ilmenite documented by Craddock et al., (2010) but our results suggest that it is unlikely to reflect equilibrium conditions, and other processes such as diffusion or inheritance of isotopes from pre-existing minerals have to be invoked.

5.3. Titanium isotopic fractionation by hydrodynamic sorting during sediment transport

Titanium isotopic system has been used to reconstruct the chemical evolution of the continental crust in Earth's history (Greber et al., 2017b; Deng et al., 2019), relying on the fact that the Ti isotopic composition of igneous rocks changes during magmatic differentiation (Millet et al., 2016; Johnson et al., 2019; Aarons et al., 2020; Hoare et al., 2020; Wang et al., 2020a; Zhao et al., 2020). Titanium is often considered to be immobile under terrestrial surface conditions and thus is used for normalizing concentrations of water-soluble elements (*e.g.*, Brimhall and Dietrich, 1987; Sheldon and Tabor, 2009), therefore Ti isotopic fractionation is expected to be insignificant during low temperature weathering processes. However, using Ti isotopes of detrital rocks such as shales to reconstruct the composition of the continental crust through time, as has been done in Greber et al. (2017b), relies on the premise that Ti isotopes do not fractionate during transport and sedimentation processes so that the Ti isotopic compositions of bulk sediments can reflect the integrated compositions of the sources. Sedimentary processes involve weathering, mixing, and transport of minerals, which can involve hydrodynamic sorting. Insoluble elements such as Ti, Al, and Zr, although resistant to chemical weathering, can potentially be fractionated relative to their source abundances by hydrodynamic sorting during fluvial transport (Garcia et al., 1994; Bouchez et al., 2011; Lupker et al., 2011; Garzanti et al., 2011). Previous study of river sediments showed that elemental compositions of river suspended sediments changed as a function of sampling depth or grain size due to hydrodynamic sorting (Bouchez et al., 2011; Garzanti et al., 2011). For example, a trend of increasing Ti/Th (Th was considered to be insoluble and was used as the normalization element) with decreasing Al/Si (a surrogate for grain size) in Amazon river suspended sediments was found by Bouchez et al. (2011), and was interpreted as reflecting hydrodynamic sorting of Ti-rich heavy minerals into the near bottom of the water channel (*i.e.*, low Al/Si coarse samples).

If fluvial transport can fractionate insoluble elements including Ti, the question arises that whether it could also fractionate Ti isotopes and induce a shift between the Ti isotopic composition of sediments (*e.g.*, river sediments and shales) and their source, complicating the use of the Ti isotopic composition of shales as a proxy for the upper continental crust composition (Greber et al., 2017b). In shales, a strong correlation between TiO_2 and Al_2O_3 has long been observed (*e.g.*, Goldschmidt, 1954; Garcia et al., 1994; Totten and Hanan, 2007), which is often attributed to the retention of Ti within the fine-grained clay minerals, but heavy Ti-rich minerals such as ilmenite and rutile also contribute to Ti budget of suspended loads in rivers, because on the TiO_2 *vs.* Al_2O_3 plot, the TiO_2 value of shales is greater than zero at zero Al_2O_3 (Totten and Hanan,

Table 10
Parameters used for calculating Fe and Mg isotopic co-evolution during the anatexis of metapelitic rocks.

Parameters	Comments
$Fe_{Grt\ produced}/Fe_{Bt\ consumed} = 0.75$	75% Fe consumed in biotite during reaction enters product garnet; Calculated based on the stoichiometry of the reaction (Eq. (12)) and the chemical formulas of biotite and garnet
$(Mg/Fe)_{Bt} = 1$	Initial molar Fe/Mg ratio of biotite; Assuming the ratio is similar to Moosilauke biotite (Hodges and Spear, 1982)
$K_D^{Fe-Mg}{}_{Grt-Bt} = \frac{X_{Grt}^{Fe}}{X_{Grt}^{Mg}} / \frac{X_{Bt}^{Fe}}{X_{Bt}^{Mg}} = 2.63$	Fe-Mg distribution coefficient between garnet and biotite at 850 °C and 10 kbar (Breton and Thompson, 1988)
$K_D^{Fe-Mg}{}_{Grt-Melt} = \frac{X_{Grt}^{Fe}}{X_{Grt}^{Mg}} / \frac{X_{Melt}^{Fe}}{X_{Melt}^{Mg}} = 2.32$	Fe-Mg distribution coefficient between garnet and melt at 850 °C and 10 kbar (Breton and Thompson, 1988)
$\Delta^{56}Fe_{Melt\text{-}Bt} = 0.22‰$	Fe isotope fractionation between melt (heavy) and biotite (light) at 850 °C; see Section 5.1 for more information
$\Delta^{56}Fe_{Bt\text{-}Grt} = 0.15‰$	Fe isotope fractionation between biotite (heavy) and garnet (light) at 850 °C; Calculated by extrapolating Fe isotope fractionation between Moosilauke biotite and garnet to 850 °C
$\Delta^{26}Mg_{Melt\text{-}Bt} = 0.97‰$	Mg isotope fractionation between melt (heavy) and biotite (light); Assuming $\Delta^{26}Mg_{Melt\text{-}Bt}/\Delta^{56}Fe_{Melt\text{-}Bt} = \Delta^{26}Mg_{Bt\text{-}Grt}/\Delta^{56}Fe_{Bt\text{-}Grt}$ (see Section 5.1)
$\Delta^{26}Mg_{Bt\text{-}Grt} = 0.66‰$	Mg isotope fractionation between biotite (heavy) and garnet (light); Through extrapolation of Mg isotope fractionation between Moosilauke biotite and garnet to 850 °C

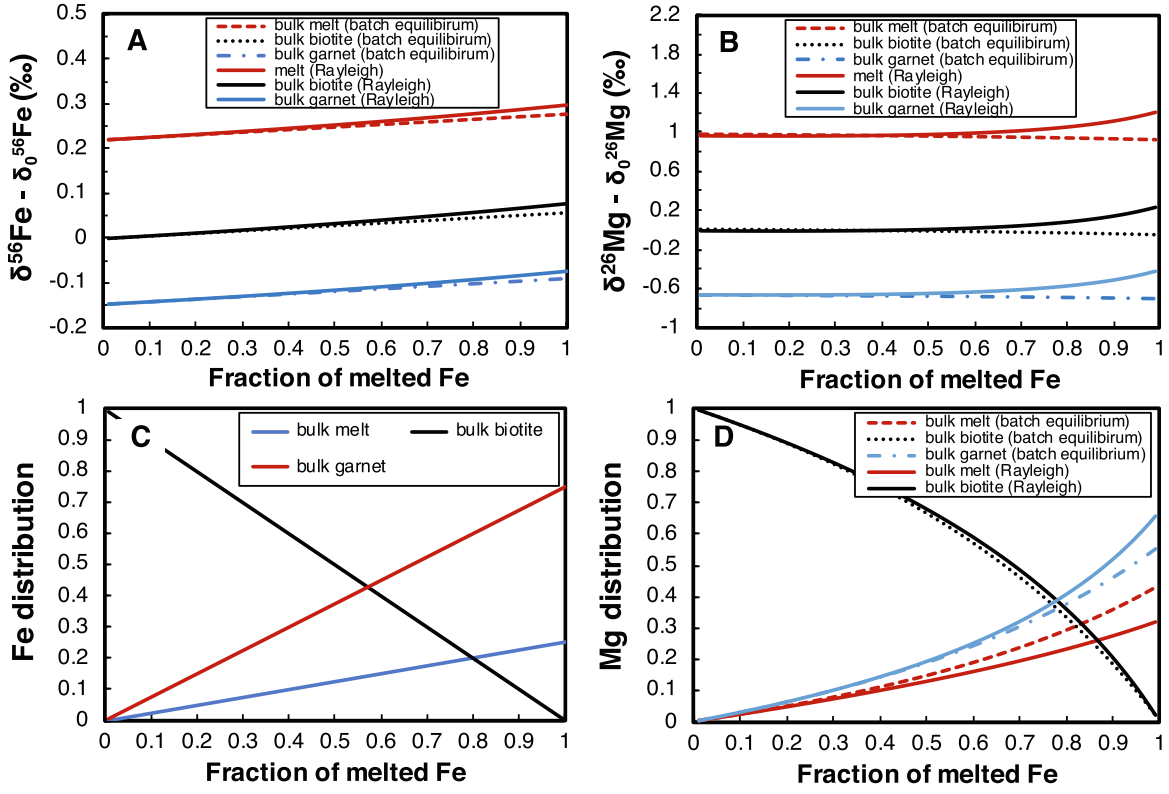

Fig. 9. Iron and Mg distribution and isotopic evolution during biotite dehydration melting. Elemental partitioning and isotopic fractionation are considered between three phases of biotite, garnet and melt. The initial Fe and Mg isotopic compositions of the source are noted as $\delta_0^{56}Fe$ and $\delta_0^{26}Mg$. Fe distribution was assumed to follow the stoichiometry of the biotite breakdown reaction (Eq. (12)). Mg distribution was assumed to be governed by Fe-Mg exchange coefficients among the three phases. (A) Iron isotopic evolution of biotite, garnet and melt during biotite dehydration melting, calculated for both batch equilibrium (dashed lines) and Rayleigh fractionation (solid lines) scenarios. (B) Magnesium isotopic evolution for biotite, garnet and melt. (C) Iron distribution among biotite, garnet, and melt during biotite dehydration melting. (D) Magnesium distribution among biotite, garnet, and melt during biotite dehydration melting.

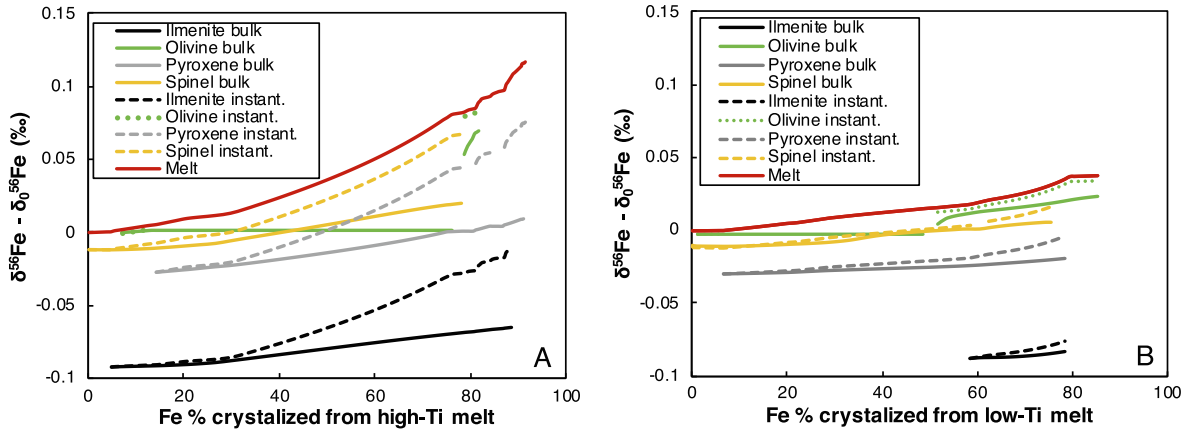

Fig. 10. Iron isotopic compositions of minerals and melt during crystallization of average high-Ti mare basalt composition (A) and average low-Ti mare basalt composition (B). The mineral crystallization sequence was calculated using MELTS program, and the equilibrium Fe isotope fractionation factors between minerals are calculated using the force constants listed in Table S3. The results suggest that the Fe isotopic compositions of ilmenite (either instantaneously crystallized or bulk average) are always lighter than the Fe isotopic compositions of pyroxene and olivine during melt crystallization, which is at odds with the observed heavy Fe isotopic composition of ilmenite in mare basalts. This implies that ilmenite must have experienced non-equilibrium isotope fractionation processes.

2007). Further work is needed to identify the carrier of Ti in rivers, and in particular whether Ti in the finest size fraction is in clay minerals or in secondary Ti-oxides. We assume below that clay minerals and coarser Ti-rich oxides are the two main Ti carriers in sediments. Given that biotite and clay minerals are both phyllosilicates with the same flat sheet crystal structure, biotite may be used as a proxy for clay minerals with regard to Ti equilibrium isotope fractionation. Our study suggests that at equilibrium, biotite should be preferentially enriched in the heavy Ti isotopes compared to ilmenite (Section 4.3). Many other silicate minerals are also expected to have heavy Ti isotopic compositions relative to ilmenite, because ilmenite and Ti-bearing oxides host Ti in a higher coordination than silicates (Millet et al., 2016; Johnson et al., 2019; Wang et al., 2020a). Regardless of whether Ti is fractionated at equilibrium during clay formation or clay formation simply inherits the Ti isotopic composition of primary silicate minerals (*e.g.*, biotite and pyroxene), we would expect these clay minerals to have heavy Ti isotopic composition relative to Ti-bearing oxides. It is thus conceivable that hydrodynamic sorting in fluvial systems, which would remove Ti-rich heavy minerals into coarse-grained sediments, would enrich fine-grained rafting clay minerals in heavy Ti isotopic composition, and thus would lead to a heavier Ti isotopic composition in shales than source materials.

The effect of sorting on fractionating Ti isotopic compositions of river sediments and shales can be broadly constrained using the observed Ti isotope fractionation between biotite and ilmenite. In Fig. 10, we use the Ti isotopic fractionation between biotite and ilmenite constrained in this study as a proxy to estimate the isotopic composition of sediments due to mixing of clay minerals and Ti-bearing oxide minerals. Assuming an isotopic fractionation between clay minerals and Ti-oxide minerals of +0.35‰ (the fractionation observed in Moosilauke biotite and ilmenite; Section 4.3), and a Ti/Al ratio of 0.04 (mol/mol) for clay

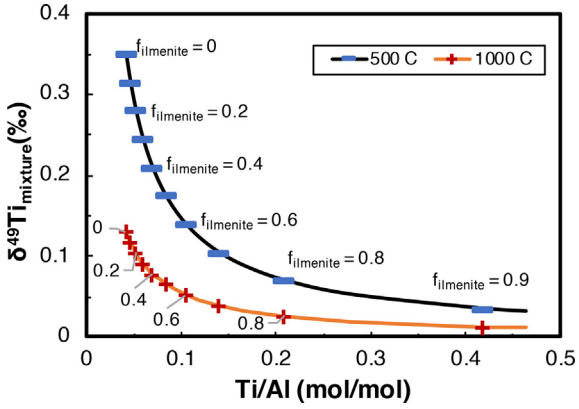

Fig. 11. Titanium isotopic composition of sediments modeled by assuming a two-endmember mixing between Ti-rich heavy minerals (using ilmenite as a proxy, assuming no Al in ilmenite and its isotopic composition of zero) and clay minerals (using biotite as a proxy, assuming a a Ti/Al mol/mol ratio of 0.04, and a δ^{49}Ti value heavier than ilmenite by 0.35‰ at 500 °C and by 0.13‰ at 1000 °C).

minerals (similar to Moosilauke biotite) and no Al in Ti-rich minerals (similar to Moosilauke ilmenite), Ti isotopic compositions of sediments as a function of their Ti/Al ratios is calculated by mixing the two components (assuming ilmenite has a Ti isotopic composition of zero). A smaller fractionation of +0.13‰ at a higher temperature (1000 °C) corresponding to magmatic conditions is also shown in Fig. 11 for comparison. These fractionations would represent the largest possible Ti isotopic variations between sediments and their sources. In reality, the fractionation would be smaller given that the two endmembers of Fe-Ti oxides and phyllosilicates are mixed to some levels in both the sources and sediments. Further detailed work

on the Ti isotopic compositions, Ti mineral carriers, and Ti/Al ratios of river sediments and shales will tell us more quantitatively whether such fractionation needs to be accounted for in provenance reconstructions. Our data suggest that the Ti isotopic difference between sediments and their sources most likely will not exceed 0.35‰.

6. CONCLUSION

Three independent methods have been used in this study for constraining equilibrium Fe isotope fractionation factors among several common rock-forming minerals, including (*i*) isotopic analyses of minerals from Mt. Moosilauke (garnet, ilmenite, biotite, tourmaline, muscovite, plagioclase and quartz; Table 1 and Fig. 2), (*ii*) NRIXS measurements of Fe force constants of natural almandine, ilmenite, annite, schorl and fayalite (Table 3 and Fig. 6), and (*iii*) *ab initio* calculations of Fe force constants of almandine, ilmenite, annite, schorl and fayalite (Table 4 and Fig. 6). Given that Fe^{3+} content has a large influence on the Fe-O bond strength and hence isotopic fractionation, Mössbauer spectroscopy was performed to quantify the $Fe^{3+}/\Sigma Fe$ ratios in the natural minerals measured by NRIXS (Fig. 4 and Table 6). Equilibrium Fe isotopic fractionation factors between pure Fe^{2+}-endmember minerals are calculated after applying a correction to account for the contribution of Fe^{3+}. In general, the three methods show good consistency for Fe isotopes (Fig. 7 and Table 8), suggesting that Moosilauke minerals have reached Fe isotope equilibrium.

By comparing to Fe isotopic fractionations in Moosilauke minerals and Mg and Ti isotopic fractionations reported in literature, we show that Moosilauke minerals are also in isotopic equilibrium for Mg and Ti isotopes. We report equilibrium Mg isotope fractionation factors between biotite, tourmaline, and garnet, as well as equilibrium Ti isotope fractionation factor between biotite and ilmenite (Table 8). Several applications of the newly constrained equilibrium isotopic fractionation factors are discussed: (*i*) Fe and Mg isotope fractionation during anatexis of metapelites was modeled and the results are compared with previous migmatite measurements, (*ii*) the Fe isotope fractionation factors between ilmenite and other minerals suggest that the ilmenite in mare basalts must have crystalized in disequilibrium with other minerals and melt, and (*iii*) hydrodynamic sorting during fluvial transport of Ti-oxides could potentially fractionate the Ti isotopic composition of terrigenous sediments, and further work is needed to tell if this is an issue in provenance studies.

Declaration of Competing Interest

The authors declare that they have no known competing financial interests or personal relationships that could have appeared to influence the work reported in this paper.

ACKNOWLEDGEMENTS

We thank Marc Blanchard for insightful discussions on the DFT approach and his assistance in addressing some comments from the reviewers. This work was supported by grants from NASA (NNX17AE86G, NNX17AE87G, 80NSSC17K0744, and 80NSSC20K0821) and NSF (EAR1502591, EAR144495, and EAR-2001098) to ND, by a NASA Earth and Space Science Fellowship NNX15AQ97H and a Carnegie Postdoctoral Fellowship to NXN. This research used resources of the Advanced Photon Source, a U.S. Department of Energy (DOE) Office of Science User Facility operated for the DOE Office of Science by Argonne National Laboratory under Contract No. DE-AC02-06CH11357.

APPENDIX A. SUPPLEMENTARY DATA

Supplementary data to this article can be found online at https://doi.org/10.1016/j.gca.2021.03.014.

REFERENCES

Aarons S. M., Reimink J. R., Greber N. D., Heard A. W., Zhang Z. and Dauphas N. (2020) Titanium isotopes constrain a magmatic transition at the Hadean-Archean boundary in the Acasta Gneiss Complex. *Sci. Adv.* **6**, eabc9959.

Alp E. E., Sturhahn W., Toellner T. S., Zhao J., Hu M. and Brown D. E. (2003) Vibrational dynamics studies by nuclear resonant inelastic X-ray scattering. In *Mössbauer Spectroscopy*. Springer, pp. 3–20.

Alvarez M., Sileo E. E. and Rueda E. H. (2008) Structure and reactivity of synthetic Co-substituted goethites. *Am. Mineral.* **93**, 584–590.

Amthauer G., Annerste H. and Hafner S. S. (1976) The Mössbauer spectrum of 57Fe in silicate garnets. *Zeitschrift für Kristallographie-Crystall. Mater.* **143**, 14–55.

Annersten H. (1974) Mössbauer studies of natural biotites. *Am. Mineral.: J. Earth Planet. Mater.* **59**, 143–151.

Bačík P., Uher P., Ertl A., Jonsson E., Nysten P., Kanický V. and Vaculovič T. (2012) Zoned Ree enriched dravite from a granitic pegmatite in Forshammar Bergslagen Province, Sweden an Empa Xrd and La–Icp-Ms Study. *Can. Mineral.* **50**, 825–841.

Basciano L. C. and Peterson R. C. (2007) Jarosite–hydronium jarosite solid-solution series with full iron site occupancy: mineralogy and crystal chemistry. *Am. Mineral.* **92**, 1464–1473.

Beard B. L., Handler R. M., Scherer M. M., Wu L., Czaja A. D., Heimann A. and Johnson C. M. (2010) Iron isotope fractionation between aqueous ferrous iron and goethite. *Earth Planet. Sci. Lett.* **295**, 241–250.

Beard B. L. and Johnson C. M. (2004) Inter-mineral Fe isotope variations in mantle-derived rocks and implications for the Fe geochemical cycle. *Geochim. Cosmochim. Acta* **68**, 4727–4743.

Bigeleisen J. and Mayer M. G. (1947) Calculation of equilibrium constants for isotopic exchange reactions. *J. Chem. Phys.* **15**(5), 261–267.

Blanchard M., Poitrasson F., Méheut M., Lazzeri M., Mauri F. and Balan E. (2009) Iron isotope fractionation between pyrite (FeS2), hematite (Fe2O3) and siderite (FeCO3): A first-principles density functional theory study. *Geochim. Cosmochim. Acta* **73**, 6565–6578.

Blanchard M., Dauphas N., Hu M. Y., Roskosz M., Alp E. E., Golden D. C., Sio C. K., Tissot F. L. H., Zhao J., Gao L., Morris R. V., Fornace M., Floris A., Lazzeri M. and Balan E. (2015) Reduced partition function ratios of iron and oxygen in goethite. *Geochim. Cosmochim. Acta* **151**, 19–33.

Blanchard M., Balan E. and Schauble E. A. (2017) Equilibrium fractionation of non-traditional isotopes: a molecular modeling perspective. *Rev. Mineral. Geochem.* **82**, 27–63.

Bouchez J., Gaillardet J., France-Lanord C., Maurice L. and Dutra-Maia P. (2011) Grain size control of river suspended sediment geochemistry: Clues from Amazon River depth profiles. *Geochem., Geophys., Geosyst.* **12**.

Breton N. L. and Thompson A. B. (1988) Fluid-absent (dehydration) melting of biotite in metapelites in the early stages of crustal anatexis. *Contr. Mineral. Petrol.* **99**, 226–237.

Brimhall G. H. and Dietrich W. E. (1987) Constitutive mass balance relations between chemical composition, volume, density, porosity, and strain in metasomatic hydrochemical systems: results on weathering and pedogenesis. *Geochim. Cosmochim. Acta* **51**, 567–587.

Brown M. (2013) Granite: From genesis to emplacement. *GSA Bull.* **125**, 1079–1113.

Brown M. and Rushmer T. (2006) *Evolution and Differentiation of the Continental Crust*. Cambridge University Press.

Chumakov A. I. and Sturhahn W. (1999) Experimental aspects of inelastic nuclear resonance scattering. *Hyperfine Interact.* **123**, 781–808.

Clemens J. D. (2006) *Melting of the Continental Crust: Fluid Regimes, Melting Reactions, and Source-Rock Fertility*. Cambridge University Press.

Clemens J. D. and Vielzeuf D. (1987) Constraints on melting and magma production in the crust. *Earth Planet. Sci. Lett.* **86**, 287–306.

Craddock P. R. and Dauphas N. (2010) Iron isotopic compositions of reference materials, geostandards and chondrites. *Geostand. Geoanal. Res* **35**, 101–123.

Craddock P. R., Dauphas N. and Clayton R. N. (2010) Mineralogical control on iron isotopic fractionation during lunar differentiation and magmatism. In Lunar and Planetary Science Conference p. 1230.

Dauphas N., Janney P. E., Mendybaev R. A., Wadhwa M., Richter F. M., Davis A. M., Van Zuilen M., Hines R. and Foley C. N. (2004) Chromatographic separation and multicollection-ICPMS analysis of iron. Investigating mass-dependent and-independent isotope effects. *Anal. Chem.* **76**, 5855–5863.

Dauphas N., Pourmand A. and Teng F.-Z. (2009) Routine isotopic analysis of iron by HR-MC-ICPMS: How precise and how accurate? *Chem. Geol.* **267**, 175–184.

Dauphas N., Roskosz M., Alp E. E., Golden D. C., Sio C. K., Tissot F. L. H., Hu M. Y., Zhao J., Gao L. and Morris R. V. (2012) A general moment NRIXS approach to the determination of equilibrium Fe isotopic fractionation factors: application to goethite and jarosite. *Geochim. Cosmochim. Acta* **94**, 254–275.

Dauphas N., Roskosz M., Alp E. E., Neuville D. R., Hu M. Y., Sio C. K., Tissot F. L. H., Zhao J., Tissandier L., Médard E. and Cordier C. (2014) Magma redox and structural controls on iron isotope variations in Earth's mantle and crust. *Earth Planet. Sci. Lett.* **398**, 127–140.

Dauphas N., John S. G. and Rouxel O. (2017) Iron isotope systematics. *Rev. Mineral. Geochem.* **82**, 415–510.

Dauphas N., Hu M. Y., Baker E. M., Hu J., Tissot F. L., Alp E. E., Roskosz M., Zhao J., Bi W. and Liu J. (2018) SciPhon: a data analysis software for nuclear resonant inelastic X-ray scattering with applications to Fe, Kr, Sn, Eu and Dy. *J. Synchrotron Radiation* **25**, 1581–1599.

Dauphas N. and Rouxel O. (2006) Mass spectrometry and natural variations of iron isotopes. *Mass Spectrom. Rev.* **25**, 515–550.

Deng Z., Chaussidon M., Savage P., Robert F., Pik R. and Moynier F. (2019) Titanium isotopes as a tracer for the plume or island arc affinity of felsic rocks. *Proc. Natl. Acad. Sci.* **116**, 1132–1135.

Domeneghetti M. C., Molin G. M., Stimpfl M. and Tribaudino M. (1995) Orthopyroxene from the Serra de Magé Meteorite: Structure refinement and estimation of C2/c pyroxene contributions to apparent Pbca diffraction violations. *Am. Mineral.* **80**, 923–929.

Droop G. T. R. (1987) A general equation for estimating Fe3+ concentrations in ferromagnesian silicates and oxides from microprobe analyses, using stoichiometric criteria. *Mineral. Mag.* **51**, 431–435.

Ducher M., Blanchard M. and Balan E. (2016) Equilibrium zinc isotope fractionation in Zn-bearing minerals from first-principles calculations. *Chem. Geol.* **443**, 87–96.

Dyar M. D. and Burns R. G. (1986) Mössbauer spectral study of ferruginous one-layer trioctahedral micas. *Am. Mineral.* **71**, 955–965.

Dyar M. D., Taylor M. E., Lutz T. M., Francis C. A., Guidotti C. V. and Wise M. (1998) Inclusive chemical characterization of tourmaline; Mossbauer study of Fe valence and site occupancy. *Am. Mineral.* **83**, 848–864.

El Goresy A., Ramdohr P., Medenbach O. and Bernhardt H.-J. (1974) Taurus-Littrow TiO2-rich basalts-Opaque mineralogy and geochemistry. In Lunar and Planetary Science Conference Proceedings pp. 627–652.

Elardo S. M. and Shahar A. (2017) Non-chondritic iron isotope ratios in planetary mantles as a result of core formation. *Nat. Geosci.* **10**, 317–321.

Ferrow E. A., Annersten H. and Gunawardane R. P. (1988) Mössbauer effect study on the mixed valence state of iron in tourmaline. *Mineral. Mag.* **52**, 221–228.

Fjellvåg H., Grønvold F., Stølen S. and Hauback B. (1996) On the crystallographic and magnetic structures of nearly stoichiometric iron monoxide. *J. Solid State Chem.* **124**, 52–57.

Fortier S. and Donnay G. (1975) Schorl refinement showing composition dependence of the tourmaline structure. *Can. Mineral.* **13**, 173–177.

Fujii T., Moynier F., Blichert-Toft J. and Albarède F. (2014) Density functional theory estimation of isotope fractionation of Fe, Ni, Cu, and Zn among species relevant to geochemical and biological environments. *Geochim. Cosmochim. Acta* **140**, 553–576.

Garcia D., Fonteilles M. and Moutte J. (1994) Sedimentary Fractionations between Al, Ti, and Zr and the Genesis of Strongly Peraluminous Granites. *J. Geol.* **102**, 411–422.

Garrity K. F., Bennett J. W., Rabe K. M. and Vanderbilt D. (2014) Pseudopotentials for high-throughput DFT calculations. *Comput. Mater. Sci.* **81**, 446–452.

Garzanti E., Andó S., France-Lanord C., Censi P., Vignola P., Galy V. and Lupker M. (2011) Mineralogical and chemical variability of fluvial sediments 2. Suspended-load silt (Ganga–Brahmaputra, Bangladesh). *Earth Planet. Sci. Lett.* **302**, 107–120.

Geiger C. A., Armbruster T., Lager G. A., Jiang K., Lottermoser W. and Amthauer G. (1992) A combined temperature dependent 57 Fe Mössbauer and single crystal X-ray diffraction study of synthetic almandine: Evidence for the Gol'danskii-Karyagin effect. *Phys. Chem. Miner.* **19**, 121–126.

Giannozzi P., Baroni S., Bonini N., Calandra M., Car R., Cavazzoni C., Ceresoli D., Chiarotti G. L., Cococcioni M. and Dabo I. (2009) QUANTUM ESPRESSO: a modular and open-source software project for quantum simulations of materials. *J. Phys.: Condens. Matter* **21** 395502.

Giannozzi P., Andreussi O., Brumme T., Bunau O., Nardelli M. B., Calandra M., Car R., Cavazzoni C., Ceresoli D. and Cococcioni M. (2017) Advanced capabilities for materials modelling with Quantum ESPRESSO. *J. Phys.: Condens. Matter* **29** 465901.

Gibb T. C., Greenwood N. N. and Twist W. (1969) The Mössbauer spectra of natural ilmenites. *J. Inorg. Nucl. Chem.* **31**, 947–954.

Goldschmidt V. M. (1954) Oxford at Clarendon Press: London. *Geochemistry* **730**.

Greber Nicolas D., Dauphas N., Bekker A., Ptáček M. P., Bindeman I. N. and Hofmann A. (2017b) Titanium isotopic evidence for felsic crust and plate tectonics 3.5 billion years ago. *Science* **357**, 1271–1274.

Greber Nicolas D., Dauphas N., Puchtel I. S., Hofmann B. A. and Arndt N. T. (2017a) Titanium stable isotopic variations in chondrites, achondrites and lunar rocks. *Geochim. Cosmochim. Acta* **213**, 534–552.

Hazen R. M. (1977) Effects of temperature and pressure on the crystal structure of ferromagnesian olivine. *Am. Mineral.* **62**, 286–295.

Henry D. J. and Guidotti C. V. (2002) Titanium in biotite from metapelitic rocks: Temperature effects, crystal-chemical controls, and petrologic applications. *Am. Mineral.* **87**, 375–382.

Henry D. J., Guidotti C. V. and Thomson J. A. (2005) The Ti-saturation surface for low-to-medium pressure metapelitic biotites: Implications for geothermometry and Ti-substitution mechanisms. *Am. Mineral.* **90**, 316–328.

Hill P. S. and Schauble E. A. (2008) Modeling the effects of bond environment on equilibrium iron isotope fractionation in ferric aquo-chloro complexes. *Geochim. Cosmochim. Acta* **72**, 1939–1958.

Hoare L., Klaver M., Saji N. S., Gillies J., Parkinson I. J., Lissenberg C. J. and Millet M.-A. (2020) Melt chemistry and redox conditions control titanium isotope fractionation during magmatic differentiation. *Geochim. Cosmochim. Acta*.

Hodges K. V. and Spear F. S. (1982) Geothermometry, geobarometry and the Al2SiO5 triple point at Mt. Moosilauke, New Hampshire. *Am. Mineral.* **67**, 1118–1134.

Holdaway M. J. (1971) Stability of andalusite and the aluminosilicate phase diagram. *Am. J. Sci.* **271**, 97–131, doi 10.

Hu M. Y., Toellner T. S., Dauphas N., Alp E. E. and Zhao J. (2013) Moments in nuclear resonant inelastic x-ray scattering and their applications. *Phys. Rev. B* **87** 064301.

Huang F., Zhang Z., Lundstrom C. C. and Zhi X. (2011) Iron and magnesium isotopic compositions of peridotite xenoliths from Eastern China. *Geochim. Cosmochim. Acta* **75**, 3318–3334.

Huang F., Chen L., Wu Z. and Wang W. (2013) First-principles calculations of equilibrium Mg isotope fractionations between garnet, clinopyroxene, orthopyroxene, and olivine: Implications for Mg isotope thermometry. *Earth Planet. Sci. Lett.* **367**, 61–70.

Jarosewich E., Nelen J. A. and Norberg J. A. (1980) Reference samples for electron microprobe analysis. *Geostandards Newsletter* **4**, 43–47.

Johnson A. C., Aarons S. M., Dauphas N., Nie N. X., Zeng H., Helz R. T., Romaniello S. J. and Anbar A. D. (2019) Titanium isotopic fractionation in Kilauea Iki lava lake driven by oxide crystallization. *Geochim. Cosmochim. Acta* **264**, 180–190.

Kesson S. E. and Ringwood A. E. (1976) Mare basalt petrogenesis in a dynamic moon. *Earth Planet. Sci. Lett.* **30**, 155–163.

Kowalski P. M. and Jahn S. (2011) Prediction of equilibrium Li isotope fractionation between minerals and aqueous solutions at high P and T: An efficient ab initio approach. *Geochim. Cosmochim. Acta* **75**, 6112–6123.

Kowalski P. M., Wunder B. and Jahn S. (2013) Ab initio prediction of equilibrium boron isotope fractionation between minerals and aqueous fluids at high P and T. *Geochim. Cosmochim. Acta* **101**, 285–301.

Lavina B., Cesare B., Álvarez-Valero A. M., Uchida H., Downs R. T., Koneva A. and Dera P. (2009) Closure temperatures of intracrystalline ordering in anatectic and metamorphic hercynite, Fe2+ Al2O4. *Am. Mineral.* **94**, 657–665.

Lavina B., Dera P., Downs R. T., Yang W., Sinogeikin S., Meng Y., Shen G. and Schiferl D. (2010) Structure of siderite FeCO 3 to 56 GPa and hysteresis of its spin-pairing transition. *Phys. Rev. B* **82** 064110.

Lejaeghere K., Bihlmayer G., Björkman T., Blaha P., Blügel S., Blum V., Caliste D., Castelli I. E., Clark S. J. and Dal Corso A. (2016) Reproducibility in density functional theory calculations of solids. *Science* **351**, aad3000.

Li W.-Y., Teng F.-Z., Ke S., Rudnick R. L., Gao S., Wu F.-Y. and Chappell B. W. (2010) Heterogeneous magnesium isotopic composition of the upper continental crust. *Geochim. Cosmochim. Acta* **74**, 6867–6884.

Liu Y., Spicuzza M. J., Craddock P. R., Day J. M., Valley J. W., Dauphas N. and Taylor L. A. (2010) Oxygen and iron isotope constraints on near-surface fractionation effects and the composition of lunar mare basalt source regions. *Geochim. Cosmochim. Acta* **74**, 6249–6262.

Lupker M., France-Lanord C., Lavé J., Bouchez J., Galy V., Métivier F., Gaillardet J., Lartiges B. and Mugnier J.-L. (2011) A Rouse-based method to integrate the chemical composition of river sediments: Application to the Ganga basin. *J. Geophys. Res. Earth Surf.* **116**.

Maslen E. N., Streltsov V. A., Streltsova N. R. and Ishizawa N. (1994) Synchrotron X-ray study of the electron density in α-Fe2O3. *Acta Crystallograph. Section B* **50**, 435–441.

Millet M.-A. and Dauphas N. (2014) Ultra-precise titanium stable isotope measurements by double-spike high resolution MC-ICP-MS. *J. Anal. At. Spectrom.* **29**, 1444–1458.

Millet M.-A., Dauphas N., Greber N. D., Burton K. W., Dale C. W., Debret B., Macpherson C. G., Nowell G. M. and Williams H. M. (2016) Titanium stable isotope investigation of magmatic processes on the Earth and Moon. *Earth Planet. Sci. Lett.* **449**, 197–205.

Mills S. J., Nestola F., Kahlenberg V., Christy A. G., Hejny C. and Redhammer G. J. (2013) Looking for jarosite on Mars: The low-temperature crystal structure of jarosite. *Am. Mineral.* **98**, 1966–1971.

Monkhorst H. J. and Pack J. D. (1976) Special points for Brillouin-zone integrations. *Phys. Rev. B* **13**, 5188.

Ottonello G. and Zuccolini M. V. (2009) Ab-initio structure, energy and stable Fe isotope equilibrium fractionation of some geochemically relevant H-O–Fe complexes. *Geochim. Cosmochim. Acta* **73**, 6447–6469.

Papike J. J., Hodges F. N., Bence A. E., Cameron M. and Rhodes J. M. (1976) Mare basalts: Crystal chemistry, mineralogy, and petrology. *Rev. Geophys.* **14**, 475–540.

Patiño Douce A. E. and Johnston A. D. (1991) Phase equilibria and melt productivity in the pelitic system: implications for the origin of peraluminous granitoids and aluminous granulites. *Contr. Mineral. Petrol.* **107**, 202–218.

Pattison D. R. (1992) Stability of andalusite and sillimanite and the Al_2SiO_5 triple point: constraints from the Ballachulish aureole, Scotland. *J. Geol.* **100**, 423–446.

Perdew J. P., Burke K. and Ernzerhof M. (1996) Generalized gradient approximation made simple. *Phys. Rev. Lett.* **77**, 3865.

Poitrasson F., Halliday A. N., Lee D.-C., Levasseur S. and Teutsch N. (2004) Iron isotope differences between Earth, Moon, Mars and Vesta as possible records of contrasted accretion mechanisms. *Earth Planet. Sci. Lett.* **223**, 253–266.

Polyakov V. B., Clayton R. N., Horita J. and Mineev S. D. (2007) Equilibrium iron isotope fractionation factors of minerals: Reevaluation from the data of nuclear inelastic resonant X-ray scattering and Mössbauer spectroscopy. *Geochim. Cosmochim. Acta* **71**, 3833–3846.

Polyakov V. B. and Mineev S. D. (2000) The use of Mössbauer spectroscopy in stable isotope geochemistry. *Geochim. Cosmochim. Acta* **64**, 849–865.

Polyakov V. B., Mineev S. D., Clayton R. N., Hu G. and Mineev K. S. (2005) Determination of tin equilibrium isotope fractionation factors from synchrotron radiation experiments. *Geochim. Cosmochim. Acta* **69**, 5531–5536.

Pourmand A., Dauphas N. and Ireland T. J. (2012) A novel extraction chromatography and MC-ICP-MS technique for rapid analysis of REE, Sc and Y: Revising CI-chondrite and Post-Archean Australian Shale (PAAS) abundances. *Chem. Geol.* **291**, 38–54.

Prandini G., Marrazzo A., Castelli I. E., Mounet N. and Marzari N. (2018) Precision and efficiency in solid-state pseudopotential calculations. *npj Comput. Mater.* **4**, 1–13.

Prissel K. B., Krawczynski M. J., Nie N. X., Dauphas N., Couvy H., Hu M. Y., Alp E. E. and Roskosz M. (2018) Experimentally determined effects of olivine crystallization and melt titanium content on iron isotopic fractionation in planetary basalts. *Geochim. Cosmochim. Acta* **238**, 580–598.

Rancourt D. G., Christie I. A. D., Lamarche G., Swainson I. and Flandrois S. (1994) Magnetism of synthetic and natural annite mica: ground state and nature of excitations in an exchange-wise two-dimensional easy-plane ferromagnet with disorder. *J. Magn. Magn. Mater.* **138**, 31–44.

Redhammer G. J., Beran A., Schneider J., Amthauer G. and Lottermoser W. (2000) Spectroscopic and structural properties of synthetic micas on the annite-siderophyllite binary: Synthesis, crystal structure refinement, Mossbauer, and infrared spectroscopy. *Am. Mineral.* **85**, 449–465.

Roskosz M., Sio C. K. I., Dauphas N., Bi W., Tissot F. L. H., Hu M. Y., Zhao J. and Alp E. E. (2015) Spinel–olivine–pyroxene equilibrium iron isotopic fractionation and applications to natural peridotites. *Geochim. Cosmochim. Acta* **169**, 184–199.

Roskosz M., Amet Q., Fitoussi C., Dauphas N., Bourdon B., Tissandier L., Hu M. Y., Said A., Alatas A. and Alp E. E. (2020) Redox and structural controls on tin isotopic fractionations among magmas. *Geochim. Cosmochim. Acta* **268**, 42–55.

Rudnick R. L. and Gao S. (2003) *3.01 - Composition of the Continental Crust*. Pergamon, Oxford, pp. 1–64.

Rumble, III, D. (1973) Andalusite, kyanite, and sillimanite from the Mount Moosilauke region, New Hampshire. *Geol. Soc. Am. Bull.* **84**, 2423–2430.

Rustad J. R. and Dixon D. A. (2009) Prediction of iron-isotope fractionation between hematite (α-Fe2O3) and ferric and ferrous iron in aqueous solution from density functional theory. *J. Phys. Chem. A* **113**, 12249–12255.

Schauble E. A. (2004) Applying stable isotope fractionation theory to new systems. *Rev. Mineral. Geochem.* **55**, 65–111.

Schauble E. A. (2011) First-principles estimates of equilibrium magnesium isotope fractionation in silicate, oxide, carbonate and hexaaquamagnesium(2+) crystals. *Geochim. Cosmochim. Acta* **75**, 844–869.

Sedaghatpour F. and Jacobsen S. B. (2019) Magnesium stable isotopes support the lunar magma ocean cumulate remelting model for mare basalts. *Proc. Natl. Acad. Sci. USA* **116**, 73–78.

Sedaghatpour F., Teng F.-Z., Liu Y., Sears D. W. and Taylor L. A. (2013) Magnesium isotopic composition of the Moon. *Geochim. Cosmochim. Acta* **120**, 1–16.

Seto M., Yoda Y., Kikuta S., Zhang X. W. and Ando M. (1995) Observation of nuclear resonant scattering accompanied by phonon excitation using synchrotron radiation. *Phys. Rev. Lett.* **74**, 3828.

Shahar A., Elardo S. M. and Macris C. A. (2017) Equilibrium fractionation of non-traditional stable isotopes: an experimental perspective. *Rev. Mineral. Geochem.* **82**, 65–83.

Shahar A., Hillgren V. J., Horan M. F., Mesa-Garcia J., Kaufman L. A. and Mock T. D. (2015) Sulfur-controlled iron isotope fractionation experiments of core formation in planetary bodies. *Geochim. Cosmochim. Acta* **150**, 253–264.

Shahar A., Schauble E. A., Caracas R., Gleason A. E., Reagan M. M., Xiao Y., Shu J. and Mao W. (2016) Pressure-dependent isotopic composition of iron alloys. *Science* **352**, 580–582.

Shahar A., Young E. D. and Manning C. E. (2008) Equilibrium high-temperature Fe isotope fractionation between fayalite and magnetite: An experimental calibration. *Earth Planet. Sci. Lett.* **268**, 330–338.

Sheldon N. D. and Tabor N. J. (2009) Quantitative paleoenvironmental and paleoclimatic reconstruction using paleosols. *Earth Sci. Rev.* **95**, 1–52.

Skulan J. L., Beard B. L. and Johnson C. M. (2002) Kinetic and equilibrium Fe isotope fractionation between aqueous Fe (III) and hematite. *Geochim. Cosmochim. Acta* **66**, 2995–3015.

Sossi P. A. and O'Neill H. St. C. (2017) The effect of bonding environment on iron isotope fractionation between minerals at high temperature. *Geochim. Cosmochim. Acta* **196**, 121–143.

Sturhahn W., Alp E. E., Quast K. W. and Toellner T. (1999) Lamb-Möossbauer factor and second-order Doppler shift of hematite. Advanced Photon Source User Activity Report.

Sturhahn W. and Jackson J. M. (2007) Geophysical applications of nuclear resonant spectroscopy. *Spec. Papers-Geol. Soc. Am.* **421**, 157.

Sturhahn W., Toellner T. S., Alp E. E., Zhang X., Ando M., Yoda Y., Kikuta S., Seto M., Kimball C. W. and Dabrowski B. (1995) Phonon density of states measured by inelastic nuclear resonant scattering. *Phys. Rev. Lett.* **74**, 3832.

Telus M., Dauphas N., Moynier F., Tissot F. L. H., Teng F.-Z., Nabelek P. I., Craddock P. R. and Groat L. A. (2012) Iron, zinc, magnesium and uranium isotopic fractionation during continental crust differentiation: The tale from migmatites, granitoids, and pegmatites. *Geochim. Cosmochim. Acta* **97**, 247–265.

Teng F.-Z., Dauphas N. and Watkins J. M. (2017) Non-traditional stable isotopes: retrospective and prospective. *Rev. Mineral. Geochem.* **82**, 1–26.

Teng F.-Z., Li W.-Y., Ke S., Yang W., Liu S.-A., Sedaghatpour F., Wang S.-J., Huang K.-J., Hu Y. and Ling M.-X. (2015) Magnesium isotopic compositions of international geological reference materials. *Geostand. Geoanal. Res.* **39**, 329–339.

Teng F.-Z. and Yang W. (2014) Comparison of factors affecting the accuracy of high-precision magnesium isotope analysis by multi-collector inductively coupled plasma mass spectrometry. *Rapid Commun. Mass Spectrom.* **28**, 19–24.

Tian H.-C., Zhang C., Teng F.-Z., Long Y.-J., Li S.-G., He Y., Ke S., Chen X.-Y. and Yang W. (2020) Diffusion-driven extreme Mg and Fe isotope fractionation in Panzhihua ilmenite: Implications for the origin of mafic intrusion. *Geochim. Cosmochim. Acta* **278**, 361–375.

Totten M. W. and Hanan M. A. (2007) Chapter 12 Heavy Minerals in Shales. In *Developments in Sedimentology*. Elsevier, pp. 323–341.

Vielzeuf D. and Holloway J. R. (1988) Experimental determination of the fluid-absent melting relations in the pelitic system. *Contr. Mineral. Petrol.* **98**, 257–276.

Virgo D., Luth R. W., Moats M. A. and Ulmer G. C. (1988) Constraints on the oxidation state of the mantle: an electrochemical and 57Fe Mössbauer study of mantle-derived ilmenites. *Geochim. Cosmochim. Acta* **52**, 1781–1794.

Walker D., Longhi J., Stolper E. M., Grove T. L. and Hays J. F. (1975) Origin of titaniferous lunar basalts. *Geochim. Cosmochim. Acta* **39**, 1219–1235.

Wang K., Jacobsen S. B., Sedaghatpour F., Chen H. and Korotev R. L. (2015a) The earliest Lunar Magma Ocean differentiation recorded in Fe isotopes. *Earth Planet. Sci. Lett.* **430**, 202–208.

Wang S.-J., Teng F.-Z. and Bea F. (2015b) Magnesium isotopic systematics of metapelite in the deep crust and implications for granite petrogenesis. *Geochem. Persp. Lett.*, 75–83.

Wang W., Huang S., Huang F., Zhao X. and Wu Z. (2020a) Equilibrium inter-mineral titanium isotope fractionation: Implication for high-temperature titanium isotope geochemistry. *Geochim. Cosmochim. Acta* **269**, 540–553.

Wang Z.-Z., Liu S.-A., Liu Z.-C., Zheng Y.-C. and Wu F.-Y. (2020b) Extreme Mg and Zn isotope fractionation recorded in the Himalayan leucogranites. *Geochim. Cosmochim. Acta* **278**, 305–321.

Wechsler B. A. and Prewitt C. T. (1984) Crystal structure of ilmenite (FeTiO3) at high temperature and at high pressure. *Am. Mineral.* **69**, 176–185.

Wechsler B. A., Prewitt C. T. and Papike J. J. (1976) Chemistry and structure of lunar and synthetic armalcolite. *Earth Planet. Sci. Lett.* **29**, 91–103.

Welch S. A., Beard B. L., Johnson C. M. and Braterman P. S. (2003) Kinetic and equilibrium Fe isotope fractionation between aqueous Fe (II) and Fe (III). *Geochim. Cosmochim. Acta* **67**, 4231–4250.

Weyer S., Anbar A. D., Brey G. P., Münker C., Mezger K. and Woodland A. B. (2005) Iron isotope fractionation during planetary differentiation. *Earth Planet. Sci. Lett.* **240**, 251–264.

Williams K. B., Krawczynski M. J., Nie N. X., Dauphas N., Couvy H., Hu M. Y. and Alp E. E. (2016) The role of differentiation processes in mare basalt iron isotope signatures. In Lunar Planet Sci Conf p. 2779.

Wu Z., Huang F. and Huang S. (2015) Isotope fractionation induced by phase transformation: First-principles investigation for Mg2SiO4. *Earth Planet. Sci. Lett.* **409**, 339–347.

Wu H., He Y., Bao L., Zhu C. and Li S. (2017) Mineral composition control on inter-mineral iron isotopic fractionation in granitoids. *Geochim. Cosmochim. Acta* **198**, 208–217.

Yamanaka T., Komatsu Y. and Nomori H. (2007) Electron density distribution of FeTiO 3 ilmenite under high pressure analyzed by MEM using single crystal diffraction intensities. *Phys. Chem. Miner.* **34**, 307–318.

Yardley B. W. and Valley J. W. (1997) The petrologic case for a dry lower crust. *J. Geophys. Res. Solid Earth* **102**, 12173–12185.

Ye H., Wu C., Brzozowski M. J., Yang T., Zha X., Zhao S., Gao B. and Li W. (2020) Calibrating equilibrium Fe isotope fractionation factors between magnetite, garnet, amphibole, and biotite. *Geochim. Cosmochim. Acta* **271**, 78–95.

Young E. D., Manning C. E., Schauble E. A., Shahar A., Macris C. A., Lazar C. and Jordan M. (2015) High-temperature equilibrium isotope fractionation of non-traditional stable isotopes: Experiments, theory, and applications. *Chem. Geol.* **395**, 176–195.

Zhang J., Dauphas N., Davis A. M. and Pourmand A. (2011) A new method for MC-ICPMS measurement of titanium isotopic composition: Identification of correlated isotope anomalies in meteorites. *J. Anal. At. Spectrom.* **26**, 2197–2205.

Zhao X., Tang S., Li J., Wang H., Helz R., Marsh B., Zhu X. and Zhang H. (2020) Titanium isotopic fractionation during magmatic differentiation. *Contrib. Miner. Petrol.* **175**, 1–16.

Zhu D., Bao H. and Liu Y. (2015) Non-traditional stable isotope behaviors in immiscible silica-melts in a mafic magma chamber. *Sci. Rep.* **5**, 17561.

Associate editor: Fang Huang